Engineering sensitivity and spectral range of photodetection in van der Waals materials and hybrids

NANO EXPRESS

PAPER

Engineering sensitivity and spectral range of photodetection in van der Waals materials and hybrids

Shaili Sett[1], **Aparna Parappurath**[1], **Navkiranjot Kaur Gill**[1], **Neha Chauhan**[1,2] **and Arindam Ghosh**[1,3]

[1] Department of Physics, Indian Institute of Science, Bangalore 560012, India
[2] The Solid State and Structural Chemistry Unit, Indian Institute of Science, Bangalore 560012, India
[3] Centre for Nano Science and Engineering, Indian Institute of Science, Bangalore 560012, India

E-mail: shailisett@iisc.ac.in

Keywords: photoresponse, van der Waals heterostructure, 2D hybrids

OPEN ACCESS

RECEIVED
23 October 2021

REVISED
10 December 2021

ACCEPTED FOR PUBLICATION
28 December 2021

PUBLISHED
21 January 2022

Abstract

Exploration of van der Waals heterostructures in the field of optoelectronics has produced photodetectors with very high bandwidth as well as ultra-high sensitivity. Appropriate engineering of these heterostructures allows us to exploit multiple light-to-electricity conversion mechanisms, ranging from photovoltaic, photoconductive to photogating processes. These mechanisms manifest in different sensitivity and speed of photoresponse. In addition, integrating graphene-based hybrid structures with photonic platforms provides a high gain-bandwidth product, with bandwidths $\gg$ 1 GHz. In this review, we discuss the progression in the field of photodetection in 2D hybrids. We emphasize the physical mechanisms at play in diverse architectures and discuss the origin of enhanced photoresponse in hybrids. Recent developments in 2D photodetectors based on room temperature detection, photon-counting ability, integration with Si and other pressing issues, that need to be addressed for these materials to be integrated with industrial standards have been discussed.

1. Introduction

Photodetection platforms based on 2D materials and their heterostructures have progressed rapidly in the last decade and state-of-the-art detectors are at par with commercially available technologies [1, 2]. Commercially established bulk semiconductor detectors like Si, III-V semiconductors or HgCdS have certain limitations. Si is limited by its band gap for detection in the visible range, InGaAs detectors (in the NIR region) need complex processing to maintain the stoichiometric ratio while use of toxic, hazardous materials like HgCdS and HgCdTe for IR detection is harmful. NIR detectors also suffer from certain other limitations, importantly, the need for cryogenic temperatures, and poor lattice compatibility with Si. Though InGaAs can operate at ambient conditions or by thermoelectric cooling mechanism, the detector responsivity significantly improves when nitrogen-cooled. Hence, the need for new materials with ease of production, enhanced detection speed, device performance, broadband as well as selective wavelength detection, transparency and flexibility, while being compatible with existing Si technology is paramount [2, 3]. Photodetection using 2D materials has progressed from individual layers of graphene [4], transition metal dichalcogenides (TMDCs) [5–7] perovskite halide 2D crystals [8], and other 2D semiconductors [9, 10] to complex heterostructure systems combining 2D materials with plasmonic nanoparticles [11–13], quantum dots [14, 15], nanowires [16], photonic platforms [17–19], different 2D layers [20–23] as well as organic materials [24, 25]. Each individual 2D material has a unique property that has been exploited for photodetection and each offers a distinct advantage over others. While Gr allows for great electrical mobility, the van hove singularity in the optical density of states in TMDCs allows 10^7 m^{-1} absorption coefficients even in the limit of a single molecular layer, and with varying the number of layers, the band gap can be tuned. For example, monolayer Black Phosphorous (BP) has a bandgap of 1.8–2.0 eV which reduces to ~0.3 eV in bulk [26]. However, an exception to this is the layered TMDC ReS_2 which has a layer independent direct band gap of 1.5 eV [27]. In hybrids, the physical properties work in tandem to synergistically produce a better performing photodetector, though not without some trade-offs. An example of this is the

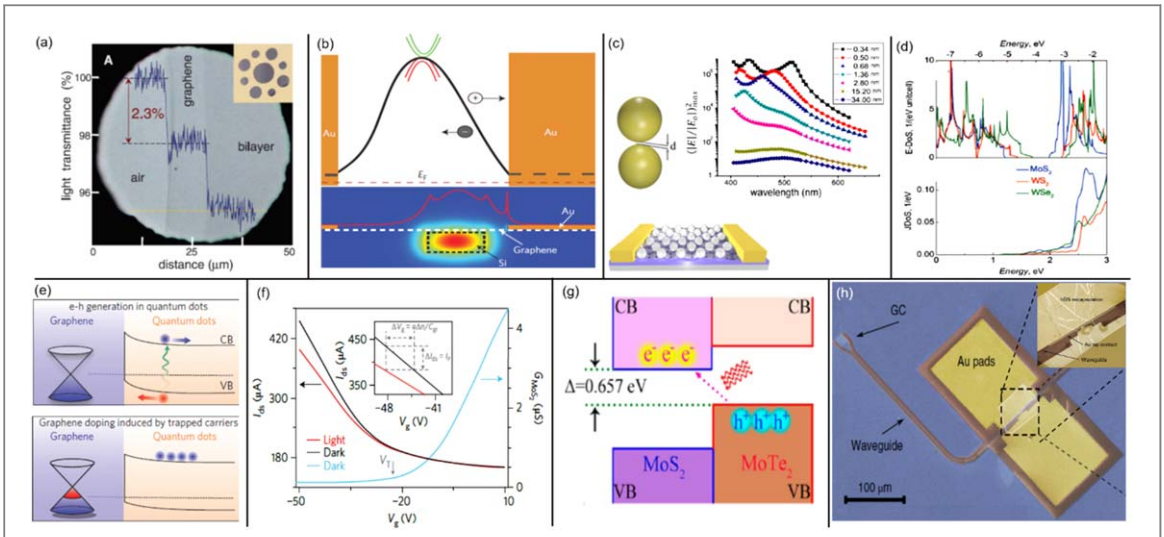

Figure 1. Pictorial representation of material and device engineering for photodetection with 2D layers. (a) Light transmittance in Gr layers. The line scan shows the intensity of transmitted white light in air, monolayer Gr and bilayer Gr. Inset shows the sample design [28]. (b) Coupling of a waveguide integrated on Gr. The potential profile (black line), shows band bending near the Au electrodes. The color plot shows simulated electric field of the transverse electric waveguide mode. The electric field intensity in the Gr channel is shown as a red line [29]. (c) Schematic of the Gr-nanoparticle hybrid device. EM field enhancement by two silver nanospheres separated by a distance d and graph showing the spectral dependence of the maximum value of $(E/E_0)^2$ at the junction for various d [30, 31]. (d) DoS for monolayer MoS_2, WS_2, and WSe_2 [32]. The JDoS for the same materials. (e) Energy level diagram of Gr/PbS Q-dot hybrid shows hole transfer to the Q-dots through a built-in field formed at the interface. On photoexcitation, holes are transferred to Gr, leaving electrons trapped in the Q-dots [15]. (f) Source–drain current (I_{ds}) versus backgate voltage (V_g) for Gr-MoS_2 heterostructure in the presence of light, and in dark [33]. The left axis of the plot shows the conductance of MoS_2 in dark. Inset shows a magnified plot at large negative value of V_g. (g) Schematic of $MoTe_2/MoS_2$ vdW heterostructures showing type-II alignment and interlayer photoexcitation [34] (h) SEM image (false color) of a vertical $MoTe_2$-Gr heterostructure detector coupled to a silicon waveguide [35].

response time in Gr-TMDC hybrids, which increases to few tens of seconds, reducing the gain-bandwidth product drastically.

This review aims to logistically explain the development of photodetectors in 2D materials and its future direction for real progress into a feasible technology. We review the physical mechanisms behind photoresponse in different van der Waals (vdW) heterostructures and explore how these hybrid materials physically function by discussing the underlying photogeneration and carrier transport mechanism. We also summarize the superiority of the vdW heterostructures from their parent counterparts, with respect to the photogeneration mechanism and the photodetection figures of merit. Finally, we present our outlook on the present research direction in 2D materials and discuss certain drawbacks in the field where future research is necessary for the progress of these materials into a marketable commodity.

1.1. Optically active hybrids with Gr and other 2D analogues

Coupling of light to the electronic excitations in 2D layers occurs via multiple pathways, which play a key role in determining the operational parameters of resulting optoelectronic devices. Gr has the most peculiar optical conductivity which is independent of any material parameters and depends only on the fine-structure constant, $\pi\alpha = 2.3\%$ over a wide wavelength range (300 nm to 2500 nm) [28]. Figure 1(a) shows the light transmittance in a monolayer of graphene, in comparison to air. Gr as a photodetector has very high bandwidth (potentially $>$ 500 GHz) with responsivity of only ~0.5 mA W^{-1} (at a gate bias of 80 V) at 1550 nm [4]. (Note: The responsivity of a photodetector is defined as the ratio of photocurrent to power falling on the detector and it is a function of wavelength.) Its ultrafast carrier dynamics, high carrier mobility and symmetric potential profile at source and drain electrodes, makes charge separation inefficient.

In figure 1 we show the integration of 2D materials with plasmonic nanoparticles, waveguides, quantum dots (Q-dots) and other 2D materials. Integrating Gr with a Fabry-Pérot microcavity increases the responsivity to 21 mA W^{-1}, three orders more than usual (with an unbiased gate electrode) due to coupling between the evanescent waveguide mode and Gr [36]. This results in ~60% absorption of light, as shown through electric field simulations in figure 1(b). Another way to enhance the electric field is to utilize plasmonic nanostructures near the contacts [12] or even sandwich a sheet of Gr between plasmonic nanoparticles [30, 31] (see figure 1(c)). Plasmonic oscillations from these nanostructures enhance the local electric field at the p–n junction formed at the interface. There is an enhancement of the photovoltage to more than twenty times in the presence of metallic nanoparticles as the electric field amplification increases strongly near the point of contact. Additionally, these

nanostructures can be designed to resonate at a particular wavelength and can be used for selective light amplification [37]. Difficulty in extracting photoelectrons can be overcome by breaking the mirror symmetry of the internal electric-field profile. one of the ways in which this has been achieved is by using different contact electrode material, where a large photocurrent is obtained, giving rise to a photoresponse of 6.1 mA W^{-1} at a wavelength of 1550 nm [38]. Besides Gr, 2D semiconductor crystals in TMDCs also offer advantages as a photodetector. In the 2D limit, the electronic bands are localized, leading to sharp peaks in the density of states (DoS) close to the conduction and valence band edges [32]. The joint density of states (JDoS) also shows a sharp rise at the conduction band edge, indicating a high probability to excite an electron–hole pair due to the availability of empty states (see figure 1(d)). They have a large optical absorption (10^7 m^{-1}) and have a bandgap in the visible range. They are mechanically strong, flexible and can sustain large strain upto ~10% before rupture [39]. Monolayer MoS_2 shows responsivity of 0.42 mA W^{-1} with a 50 ms rise time for photocurrent [5]. In this context, it is essential to introduce another important device parameter, the external quantum efficiency (*EQE*), by which the photodetector performance can be evaluated. It is defined as ratio of the number of charge carriers generated ($\frac{I_{ph}}{e}$, where $I_{ph}$is the photocurrent) to the number of incident photons ($\frac{P\lambda}{hc}$, where P is the power falling on the detector and other symbols have usual meaning) and is expressed as, $EQE = \frac{I_{ph}}{e} / \frac{P\lambda}{hc}$ TMDCs show *EQE* of 30% [32] due to their unique DoS as shown in figure 1(d). The internal quantum efficiency is an intrinsic property of the material and is defined as the product of light absorption efficiency and charge transfer efficiency [40]. IQE in TMDCs is very low (~8%) [41] due to strong exciton effects in the monolayer limit. While in graphene it lies between 6%–16% [4]. However, on integration with Q-dots, its IQE can be increased upto 18% [42] and by using quantum well hybrids, it increased to 25% [43]. MoS_2 in an electrolyte bath, with vertical charge transport, shows an IQE as high as 44% [44]. Integration of TMDCs and other 2D analogues like BP, InSe, BiTe etc with existing Gr technology such as using asymmetric electrodes [7, 45, 46], introducing plasmonic nanoparticles [47] and coupling with waveguide platforms [17, 48] have shown improved device performance.

A major breakthrough in photodetection was achieved by integrating Gr with a thin film of colloidal Q-dots [15] that paved the way for ultra-high responsivity photodetectors (shown in figure 1(e)). Light absorption is performed by the quantum dots and one type of photogenerated carriers (holes from PbS Q-dot) transfers to Gr. The oppositely charged carriers remain trapped in the Q-dot layer. This effect of photogating as we shall discuss later, leads to ultrahigh gain (~10^7). Gr–MoS_2–Gr photodetectors show an *EQE* of 55% due to efficient charge separation at the interface and a vertical device architecture [49]. Subsequently, heterostructures of graphene and TMDC (MoS_2) were achieved, which show highly sensitive photodetection of 3×10^8 A W^{-1} at room temperature, and 10^{10} A W^{-1} at 130 K, and is capable of number resolved photon detection [50, 51]. It follows the same principle of photogating as has been demonstrated by exhaustive opto-electronic measurements. An example of a typical response in the presence and absence of light, with variation in gate voltage (V_g) in Gr-MoS_2 is shown in figure 1(f). TMDC heterostructures like MoS_2/WS_2 show ultrafast charge transfer with hole transfer from MoS_2 to WS_2 within 50 fs and exciton lifetime ~ tens of ps [52]. *EQE* as high as 670% was achieved in a GeSe/$MoSe_2$ heterojunction diode with the interface playing a crucial role towards such a high efficiency [53]. Such type II semiconductor heterojunctions facilitate efficient electron–hole separation in a vertically stacked configuration with sharp atomic interfaces $MoTe_2/MoS_2$ heterostructure shows photoresponse of 0.22 A W^{-1} at 1550 nm, which is beyond the limit of their individual band gap (see figure 1(g)) [34]. Thus, it enables the design of infrared photodetectors by exploiting the interlayer excitation in vdW heterostructures.

Integration with Si photonics platforms has enabled high speed photodetection in telecommunication wavelengths. Coupling of 2D materials with a waveguide/photonic structure enhances light absorption through the evanescent field as shown through simulations in figure 1(b) [29]. Gr-based Si waveguide detectors integrated with other photocurrent enhancing elements have shown bandwidths of up to 110 GHz [11] and shall be discussed in section 4.3. Gr-$MoTe_2$ hybrid integrated on a silicon photonics platform (device architecture shown in figure 1(h)) also shows high measured bandwidth of at least 24 GHz [35].

This review explores the mechanisms behind enhanced photoresponse in 2D hybrids and functional photodetectors which have been introduced in this section. The article is arranged as follows. We provide an overview of the important photoconversion mechanisms followed by a review of each type of photodetector in its pristine and hybrid configuration. We then discuss detector performance enhancement mechanisms through both physical and chemical processes. The outlook section provides a summary of the photodetector performances in 2D materials and hybrids, followed by an in-depth discussion on important technological advances in this field. It also discusses the advantages of a 2D heterostructure as a photodetector and its superior physical properties that emerge with novel device architectures.

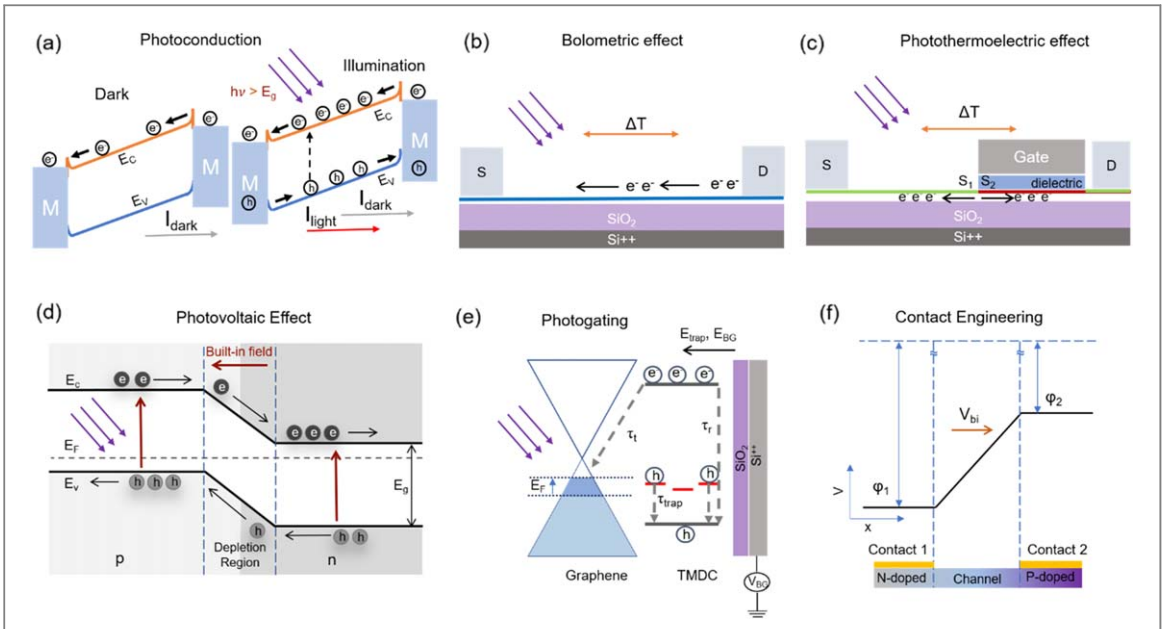

Figure 2. Schematic of major photodetection mechanisms and simulations showing photoresponse aiding mechanisms. (a) Photoconduction in a semiconductor with two metal electrodes showing creation of carriers under illumination and their separation and transport. (b) Bolometric effect: Schematic showing that a temperature gradient is created in a 2D material under illumination giving rise to a thermoelectric component. (c) Photothermoelectric effect: Schematic shows two dissimilar Seebeck coefficients in a 2D material usually created by a top-gated structure. Photocurrent is generated due to an inhomogeneous temperature gradient under illumination, giving rise to a thermo-voltage. (d) Photovoltaic effect: Schematic shows that a p-n junction creates a built-in field that separates the electrons and holes. (e) Photogating mechanism: A Gr-TMDC hybrid is shown on a SiO_2/Si substrate. Incident photon creates an e-h pair which get separated due to in-built field; traps in MoS_2 capture the holes and there is charge transfer of electrons to Gr. (f) Contact engineering: Presence of unequal Schottky barriers at the metal/semiconductor junction leads to formation of a built-in field. Details of this mechanism is discussed in section 3.2.1.

2. Key mechanisms of photodetection

In this section, we shall introduce some of the key physical mechanisms that enable conversion of light into electricity in vdW materials and hybrids.

2.1. Photoconduction

Photoconduction (PC) works on the principle of light absorption by a material that creates free carriers which are separated by applying an external bias to the semiconductor. Figure 2(a) shows a schematic of the process. Generally, in semiconductors the change in conductivity can be expressed as a simplified equation given by [54],

$$\Delta\sigma = q(\mu_n \Delta n + \mu_h \Delta p), \tag{1}$$

where $\Delta\sigma$ is the change in conductivity, q is the charge on an electron, $\mu_n(\mu_h)$is the mobility of electron (hole), Δn (Δp) is the change in carrier concentration of electrons (holes) due to illumination. The photocurrent depends on the generation and recombination rate of electron-hole (e-h) pairs and mobility of charge carriers. The transit time (τ_t), which is time required for charge carriers to reach an electrode is given by, $\tau_t = l^2/\mu V_{ds}$ [55] where l is length of the channel and V_{ds} is source-drain or bias voltage, while the carrier lifetime is given by, $\tau_l = l_r^2/D$, where, l_r is the recombination length, and D is the diffusion coefficient. The photocurrent Gain (G), which is related to the device parameter τ_t and the material parameter τ_l is then defined as, $G = \tau_l/\tau_t$. Gain can also be defined as the ratio of the photo-generated carriers per unit time (I_p) to the incident number photons of frequency (ν) in unit time ($P/h\nu$), given by [1, 55],

$$G = \frac{h\nu I_p}{eP} = \frac{h\nu}{e}\mathcal{R}, \tag{2}$$

where $\mathcal{R}$ is the responsivity, which is the ratio of the photocurrent I_p to incident power (P) and an important figure of merit for photodetectors. Another important figure of merit is the noise-equivalent-power (NEP), which characterizes the signal-to-noise ratio. It is given by, $NEP = I_n/R$, where I_n is the total current noise in the detector. An elaborate discussion on these parameters can be found in [56] .The current noise depends on the photodetection mechanism and arises from uncertainties in the photophysical mechanisms. NEP can be expressed as the minimum detectable power per square root bandwidth of a photodetector with units of $\mathrm{WHz}^{-1/2}$.

2.2. Bolometric effect

Bolometric detection is based on the change in conductance arising from temperature change induced by incident radiation as shown in figure 2(b). Detectors based on bolometric response rely on low-specific heat materials that have weak thermal interaction with the surrounding environment [57]. This increases the thermal time constant (τ_{th}), $\tau_{th} = C_{th}R_{th}$ which is the general expression for bolometric detectors where R_{th} is the thermal resistance and C_{th} is heat capacity that effectively lowers the detector bandwidth. Gr has an ultra-low electronic specific heat capacity arising from its vanishing DoS at the charge neutrality point and hence it is an ideal candidate for fast response bolometric detectors. Weak electron-phonon coupling in Gr is also advantageous in decoupling electrons from the lattice to maintain a higher electronic temperature, necessary for bolometric detection.

2.3. Photo thermoelectric effect

The production of hot charge carriers generated by incident photons resulting in a photovoltage is known as the photo-thermoelectric effect. Due to differential doping of the semiconductor, a spatially varying Seebeck coefficient produces a photovoltage, given by [2]

$$V = \int S\Delta T.dx, \tag{3}$$

where $S(x)$ is the spatially varying thermopower and ΔT is the photoinduced electronic temperature gradient. Figure 2(c) shows a schematic of a Gr photo-thermoelectric device.

2.4. Photovoltaic effect

The photovoltaic (PV) mechanism of conversion of light to split the photogenerated e-h pair relies on the formation of a p-n junction either naturally when two layers of dissimilar work function are stacked onto each other or artificially by chemical doping or through carrier modulation using a split-gate [58]. The internal built-in electric field due to the p-n junction separates the photogenerated e-h pair without any external bias. This enables photon detection at zero bias and is the driving mechanism behind self-powered devices [59]. Figure 2(d) shows the PV effect in a dissimilarly doped Gr photodetector. Such photodetectors have great potential for low-power operation with fast response required in the internet of things, wearable electronics, environmental monitoring and industrial safety. Based on device geometries, PV devices can be either lateral where the built-in electric field is parallel to the plane of the heterostructures or vertical, where the electric field is perpendicular to the plane of the device [58].

2.5. Photogating

Photogating is considered as a way of conductance modulation through a photoinduced gate voltage [40, 60]. If one type of photogenerated carrier gets trapped (due to impurity, interface states, mid-gap states etc) that prolongs their lifetime, it may be considered as an effective gate voltage since it modulates the channel conductance. The corresponding photocurrent is expressed as [60],

$$I_{ph} = \frac{\partial I_d}{\partial V_g}\Delta V_g = g_m \Delta V_g, \tag{4}$$

where I_{ph} is the change in channel current due to a change in the local gate voltage ΔV_g and g_m is the transconductance. Photogenerated carriers can also be trapped in artificially created hybrid heterostructures of 2D materials as shown in figure 2(e) for Gr-TMDC heterostructure. Light falling on the photosensitive material creates a photogenerated e-h pair, which gets separated by the local electric field formed at the junction of the two materials. This leads to photogating effect in heterostructures.

3. Photodetection in 2D materials and hybrids based on physical mechanisms

3.1. Photoconduction in 2D materials

Photoconductivity (PC) is one of the primary mechanisms of photodetection and relies on the intrinsic semiconducting property of the 2D material. In the presence of an external bias, semiconductors show PC. The response time is very fast, reaching bandwidths of ~1 GHz in high quality exfoliated 2D layers [61]. In 2D materials, the contribution of PC to the photocurrent is usually very weak and cannot be easily disentangled from other mechanisms. In 2014, Furuchi *et al* [62] reported the contribution of photoconductive and photogating effects to the photoresponse of MoS_2. Their model shows conductivity changes in MoS_2 flake in the presence and absence of trap states (figure 3(a). The photocurrent as a function of modulation frequency (3 kHz) shows a decrease in photoresponse beyond ~100 Hz. There is a background photocurrent superimposed with a smaller current that oscillates with the modulation frequency. On blocking the light, the oscillating part stops

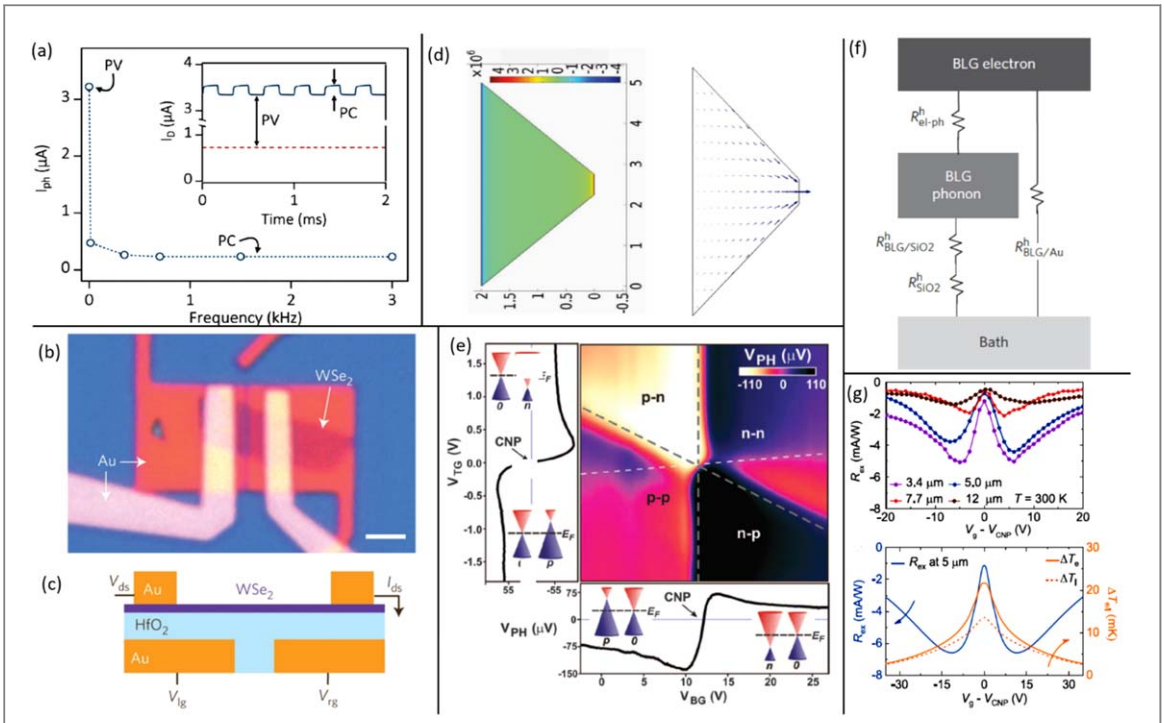

Figure 3. Photodetection in 2D heterostructures through photoconduction, photovoltaic, bolometric and photo-thermoelectric processes. (a) Photocurrent versus modulation frequency showing PC and PV effect in monolayer MoS_2 [62]. The inset shows source-drain current (I_d) versus time in the dark (red line) and under illumination (blue line). (b), (c) Local gate structure in WSe_2 in which an artificial p-n junction is created by the split-gates. An optical image and the schematic of the device [67]. (d) Color plot of simulated electric field distribution of the WSe_2 photodetector with contact length difference of 4.5 μm at zero bias and the current density distribution given alongside. The magnitude and direction of current is represented by the arrow length and direction, respectively [46]. (e) Photoresponse of dual-gated Gr p-n junction devices [68]. Spatially resolved photocurrent map at $T = 40$ K. Photovoltage (V_{PH}) versus back gate (V_{BG}) and top gate (V_T). (f) Heat conduction diagram for dual-gated bilayer Gr [69]. (g) Room temperature responsivity in high quality hBN encapsulated Gr bolometer as a function of V_g under different laser excitation wavelengths at $V_{DS} = 0.5$ V. Bottom graph shows calculated extrinsic responsivity at $\lambda = 5.0$ μm and increase in ΔT_e and ΔT_l [70].

immediately while the dominant background slowly reduces. The fast response, with $R \approx 0.06$ A W^{-1} (calculated theoretically through charge dynamics in an ideal semiconductor), is attributed to the photoconduction effect and is weakly dependent on the backgate voltage, while the slower component with higher responsivity (~6 A W^{-1}) originates from the photogating effect as shall be discussed in section 3.4. WSe_2 trilayer in a field-effect transistor (FET) configuration shows a high response of 7 A W^{-1} at −12 V back-gate voltage [63]. It has a characteristic time constant of 3.7 μs which is orders of magnitude smaller than monolayer WSe_2 (respond time is ~5 s) [64]. This larger time constant in the monolayer photodetector arises due to the influence of trap states in SiO_2, and adsorbates on the surface, which delays the response as well as alters the photophysics mechanism. A trilayer structure encompasses the issue of external traps in the system and the quick response time justifies photoconduction as the dominant mechanism for photoresponse in the device. Photoresponse in mechanically exfoliated BP in metal-semiconductor-metal configuration was investigated in the wavelength range from 1.56–3.75 μm [65]. The photocurrent ranges from 0.9–2.2 μA due to the anisotropic optical absorption coefficient in BP. Investigations by Suess *et al* [65] showed that photothermoelectricity was two orders of magnitude smaller than that of PC and contribution from bolometric and photovoltaic effect was absent. The photocurrent is dominated by photoconduction mechanism and shows a response time of 65 ps resulting in a bandwidth exceeding 1 GHz. Another study on BP shows photoresponse in the range of 1.2–5.4 μm with fall in photocurrent near 4.5 μm which corresponds to absorption edge arising from band gap values, which is attributed to photoconduction [10]. Few layered ReS_2 shows the highest photoresponse of 88600 A W^{-1} at low powers of ~10 pW [27]. It also shows broadband anisotropic light absorption, where the photocurrent can be tuned by an order of magnitude by changing the polarization of the incident beam by 90° [66]. The ultrahigh response originates due to the 1 T structure and large anisotropy in ReS_2 along with the direct band gap nature. The presence of a large Schottky barrier at the metal/ReS_2 interface also assists in additional photocurrent generation as well as suppression of dark current to ~ few pA. ReS_2 also harbors a large number (1.96×10^{13}/cm^2) of defect states due to S vacancies, that facilitates increase in the internal gain.

3.2. Photovoltaic effect in 2D junctions

The PV effect in 2D materials and hybrids have been explored in various forms. The p-n junction necessary to provide the built-in electric field, is naturally created when two dissimilar 2D materials are stacked vertically. The advantage of photodetectors that function solely based on the PV mechanism is that they have low dark current which results in a desirable *NEP*. Compared to photogating, the responsivity of PV detectors is lower since the active area of the p-n junction is small. PV detectors can operate in the photoconductive mode also, when the junction is reverse biased. A faster response time may be achieved in such a case as the junction capacitance is reduced. In individual 2D materials, a p-n junction can be artificially created as shown by Baugher *et al* [67] wherein a monolayer WSe_2 using split-gates (see figures 3(b), (c)) shows a responsivity of 210 mA W^{-1}. The split gates are used simultaneously to create NN, PP, NP and PN junctions. The NN and PP configurations are ohmic at low source-drain bias V_{ds}, while the PN and NP configurations show strongly rectifying current. Memaran *et al* [71] reported a photovoltage of 0.7–0.85 V in electrostatically gated few layer $MoSe_2$ p-n homojunction using hBN as a dielectric, which is similar to Si solar cells. Similar work has been done with other TMDCs too, like $MoTe_2$ [72] and BP [73]. Aluminium doped p-n homojunction of BP shows photovoltage of 0.14 V at telecommunication wavelengths [74] while Yu *et al* reported a lateral p-n junction using benzyl viologen as an electron dopant on p-doped BP with a responsivity of 180 mA W^{-1} and a rise time of 15 ms at 1470 nm [75]. Lateral p-n heterojunctions are difficult to manufacture since, after the growth of the first TMDC layer, the edge-front gets passivated and growth for the second film at these sites are not favourable for nucleation. Despite the challenges these heterostructures of WS_2-WSe_2 prepared by Duan *et al* [20] has been reported which shows a photovoltage of 0.47 V under an illumination wavelength of 540 nm. Li *et al* [76] prepared a WSe_2-MoS_2 p-n junction displaying a photovoltage of 0.22 V with good rectification.

2D/2D vdW heterostructures provide an opportunity for stacking different 2D materials using transfer techniques even with lattice mismatch because of weak vdW attraction between adjacent layers resulting in vertical p-n junctions. At the interface of the two layers, there is a built-in electric field induced by band alignment which immediately separates photogenerated e-h pairs resulting in a large photoresponse. Intrinsically n-type (MoS_2, WS_2, $MoSe_2$) and intrinsically p-type (WSe_2, $MoTe_2$, BP) 2D materials can be stacked together to form p-n heterojunctions [77]. WSe_2-MoS_2 [78] heterostructure has been reported to show an external efficiency of 12% at zero gate voltage proving efficient charge separation at the interface. Vertical heterostructures are better in terms of quantum efficiency because the photoactive area includes the whole overlap region rather than only the junction which is the case for lateral heterojunctions. Combining different 2D materials also provides another advantage; the electron and hole being in separate layers due to a staggered band alignment, leads to an increase in carrier lifetime which increases the responsivity. In MoS_2/$MoTe_2$ heterostructures (see figure 1(f)), K. Zhang *et al*, showed that the inter-band gap, obtained by theoretical calculations is 0.657 eV, and is beyond the limits of the intrinsic band gap of the constituent materials. Such a heterostructure shows photoresponse at a technologically important wavelength of 1550 nm. WSe_2/MoS_2 [79] heterojunction also shows a typical p-n diode behaviour and a rectification ratio of over 10^6 in reverse bias. Zero bias regime shows an open circuit voltage of around 0.3–0.4 V and short circuit current of 10–40 nA resulting in responsivity of 0.11 A W^{-1} at zero bias 0.17 A W^{-1} at a reverse bias of −1 V. Other vertical heterostructures have also been studied such as WSe_2/$MoSe_2$ [22], GaSe/$MoSe_2$ [80], BP/MoS_2 [21, 80], MoS_2/WS_2 [81] and WS_2/Bi_2Te_3 [82] show similar behaviour. Recent studies on MoS_2-ReS_2 heterostructure shows a high responsivity of 1.28 A W^{-1} in self-powered mode under an illumination wavelength of 800 nm [83]. The responsivity reaches upto ∼43 A W^{-1} at a low bias of 1 V. It has been demonstrated through spectroscopic studies that ReS_2 introduces p-doping in MoS_2, resulting in efficient extraction of charge carriers. The response time of the device is ∼20 ms, due to the effective separation of charges from the built-in electric field at the interface. $MoTe_2$-ReS_2 heterojunction, in addition, has been investigated in the NIR wavelength regime of upto 1310 nm [84]. It shows a lower responsivity of 0.1 A W^{-1} at zero bias but a higher response speed of ∼3 μs. The type II band alignment in this heterojunction is more effective in charge separation.

the Formation of double vertical heterojunctions in MoS_2/Gr/WSe_2 [85] shows a responsivity of 10^4 A W^{-1} in the visible region. Pd metal electrodes were used such that WSe_2 gets p-doped and MoS_2 n-doped resulting in a 0.23 V open-circuit voltage in zero bias condition. Here, both TMDCs and Gr contribute to the photocurrent and its wavelength range of operation is 500–2500 nm. The response time is ∼50 μs, which is due to a quick separation of the e-h pair as a result of the built-in field. Photodetectors that rely solely on the PV effect, usually have similar response times. Lastly, hybrid structures include integration of Gr with quantum dots, nanowires and perovskites, resulting in the formation of p-n junctions. These hybrid heterostructures have enhanced PV properties and along with other underlying mechanisms like photogating, show an effectively large photoresponse and will be discussed in section 3.4.

3.2.1. Engineering contacts

While the p-n junction is a necessity for the photovoltaic effect, the interface of a metal-semiconductor junction, which controls the charge injection process, is an essential component of a photodetector. It is an aiding mechanism that enhances the photoresponse. Here we shall discuss the different ways by which engineering contacts leads to a many-fold increase in photoresponse of 2D materials and hybrids.

When contacted with metal electrodes on both sides, it can be modelled as two back-to-back Schottky junctions connected with a series resistance in between. The short circuit current in the device can be expressed as [86],

$$I_{sc} = qG(A_1 W_1 - A_2 W_2) \tag{6}$$

where q is charge, G is the photo-generation rate of charge carriers, and A_1 (A_2) and W_1(W_2) are the junction area and depletion width of the first (second) Schottky junction, respectively. Breaking this symmetry to provide a self-driven current in the device forms the basis of contact engineering for self-powered photodetection. Various device structures and novel mechanisms have been proposed of which asymmetric contact geometry and asymmetric Schottky barriers (as shown in figure 2(f)) have been well researched. The asymmetric barrier heights create an in-built potential as shown in the colour plot (with inset giving the field direction).

Asymmetric metallization to break the mirror symmetry of the internal electric-field profile was shown in Gr photodetectors [38] with Pd and Ti electrodes. Since the doping resulting from different metallic contacts is different (p-type with Pd and n-type with Ti on Gr), the photocurrent near both electrodes (within 200 nm of the metal/Gr interface) can flow in the same direction, leading to an overall increase in photocurrent. Figure 3(d) shows current versus source–drain bias (V_B) with and without illumination at λ=1550 nm. The photocurrent which is the difference between the current in the device in light and dark conditions is given by the black curve. The energy band profiles in Gr shows that when V_B equals the difference in Fermi level between the palladium- and titanium-doped Gr, the potential is symmetric and photoresponse is zero. Similarly, when a semiconductor like $MoTe_2$, is contacted with Au electrodes, it shows a photoresponse of 24 mA W^{-1} at a working bias of 10 V with a 1.6 ms rise time [87] while the same 2D crystal with asymmetric contacts of n-doped and p-doped Gr [7], shows a response of 66 mA W^{-1} at a low bias of 0.2 V and with a rise time ~6 μs. In Gr/MoS_2/Gr vertical heterostructure [88] the fermi level of the bottom Gr can be adjusted which can modify the height of the Schottky barrier at the bottom Gr/MoS_2 interface This does not affect the top Gr/MoS_2 interface because of screening by MoS_2. This geometry shows a responsivity of 414 A W^{-1} and a response time of ~590 ms at 532 nm. Responsivity in the NIR region at 2000 nm is 376 A W^{-1} with a rise time of ~753 ms. The response time is far less than what is obtained in a lateral Gr/MoS_2/Gr [89], and is attributed to the small transit distance of photogenerated carriers in a vertical geometry.

Using two different electrode materials increases the complexity of processing and hence using asymmetric contact geometries (contact area or contact length) is a more viable solution. In a usual metal-TMDC-metal photodetector geometry, the metal–WSe_2 junctions have been designed to have unequal contacts lengths [46], with the difference between two contacts ranging from zero to few micrometres. The electric field distribution and current density (as shown in figure 3(d)) in the WSe_2 flake with Au/Ni electrodes and with a contact length difference of 4.5 μm shows same magnitude but opposite direction. As the contact lengths are unequal, the contact area is also unequal. Hence, there is a net short circuit current (refer to equation (6)) which aids in photovoltaic response. Self-driven photodetectors are currently being researched in other 2D analogues and hybrids [45, 90–92]

3.3. Photo-thermoelectric and Bolometric effect in Gr and TMDCs

Gr is considered to be an ideal bolometric material that offers ultra-low electronic specific heat ~10^{21} J K^{-1} and weak electron phonon-coupling while maintaining a fast response time. Jun Yan and colleagues exploited thermal decoupling of electrons from the lattice to demonstrate a dual gated bilayer Gr hot electron bolometer [69]. Electrons in Gr heat up easily on absorbing light while weak electron phonon-interaction results in a bottleneck in the heat flow path, effectively decoupling electrons from the phonon bath. This creates a change in the temperature dependent resistance of dual gated bilayer Gr, making it an excellent detector that exhibits an *NEP* of 33 fW $Hz^{-1/2}$. In this work, they have excluded the possibility of other heat loss paths like Gr to Si wafer and to electrical contacts (see figure 3(f)) by comparing the estimated thermal resistance from their experiment. A detailed study of opto-electronic measurements by Freitag *et al* [93] in biased Gr photodetectors at 200 K, demonstrated a dominant bolometric contribution to photocurrent in highly doped regimes, while the PV effect is dominant near the charge neutrality point (CNP). Recently, room temperature mid-IR bolometer using hBN encapsulated Gr device was demonstrated by Yuan *et al* [70] It shows a responsivity of 1.4 mA W^{-1} and *NEP* (11 nW $Hz^{-1/2}$), which is orders of magnitude higher than the *NEP* of the state-of-the-art microbolometers [94]. Figure 3(g) shows the responsivity as a function of back gate voltage (V_g) in Gr-encapsulated hBN bolometers. The data was modelled to self-consistently calculate the temperature elevations of ΔT_e (electronic temperature)

and ΔT_l (lattice temperature). The photocurrent was expressed as,

$$I_P = \frac{w}{L}\left\{\left[\frac{\partial\sigma}{\partial T_e}\right]_{T_e=T_s,\ T_l=T_s}\Delta T_e + \left[\frac{\partial\sigma}{\partial T_l}\right]_{T_e=T_s,\ T_l=T_s}\Delta T_l\right\} V_{ds} \quad (5)$$

where $\frac{\partial\sigma}{\partial T_e}$ and $\frac{\partial\sigma}{\partial T_l}$ are the rates of change of electrical conductivity against electron and phonon temperature respectively. The photoresponse decreases with increasing bias, due to suppression of infrared photon absorption as a result of Pauli blocking. A larger Fermi surface at large doping increases the electron-phonon scattering strength, causing greater heat dissipation. Near the CNP, there is again a reduction in photocurrent, since the two terms are smaller than that in the highly doped regime. The enhanced photoresponse in this device is attributed to the high quality of the sample by encapsulating Gr with hBN. In a different device architecture, by coupling a photonic cavity to Gr bolometer, Efetov *et al*, [95] demonstrated that, the absorption of Gr increases from 2.3% to 7%. It is based on a Johnson noise read-out that was capable of determining a thermal relaxation time of 35 ps. The *NEP* of this detector is 10 pW $Hz^{-1/2}$ at 5 K.

Gabor *et al* [68] experimentally demonstrated hot carrier assisted intrinsic photo response using dual gated single layer and bilayer Gr by exploiting the Photothermoelectric effect (PTE). The photovoltage was recorded as a function of bottom and top-gate voltages upon local laser excitation at the p-n interface. Figure 3(e) shows multiple photovoltage sign changes occurring at the interface leading to a six-fold photovoltage pattern. This characteristic photovoltage pattern of PTE effect is identified to emerge from the non-monotonic dependence of S_1 and S_2 (Seebeck coefficients of p and n region respectively) with gate voltage. Similar PTE was observed in TMDCs like WSe_2 [96] and WTe_2 [97] by differentially doping the channel using an external gate. Zhang *et al*, [98] showed that in MoS_2, through scanning photocurrent spectroscopy, hot-carrier-assisted PTE was observed in the depletion regime of a MoS_2 channel contacted by asymmetric Ti/Au electrodes. By Integrating with waveguides using a dual gate structure, PTE has been observed by Schuler *et al* [99].

3.4. Photogating in 2D materials and van der Waals hybrids

The phenomenon of photogating was first observed in single semiconductor nanowires (NWs) [100], where the surface oxide layer pins the Fermi level. This leads to band bending which causes carrier trapping at the surface and modulates the channel conductance. Band bending causes a large photoresponse of the order 10^7–10^8 A W^{-1} as observed in ZnO [100] and Ge [101] NWs. The potential barrier prevents carriers to recombine, thereby increasing the lifetime which causes persistent photocurrent (PPC) even after illumination is switched off. Similar PPC was observed in chemical vapour deposition (CVD) grown MoS_2 devices [102]. The PPC effect is weakly dependent on temperatures below 150 K, indicating freezing of carriers in the traps due to lack of thermal activation energy. It indicates that long-range Coulomb potential in MoS_2/SiO_2 is responsible for the PPC. It leads to photoresponse ~0.06 A W^{-1} with rise time of ~30 s with a decay time of 500 s, which reduces the bandwidth of the photodetector. It was observed by Furchi *et al* [62] that there is a shift in the threshold voltage (V_T) in MoS_2 phototransistors with increasing illumination intensity due to charge transfer from channel to surface-bound water molecules (see figure 4(a)). Interestingly, photocurrent (red curve) follows the transconductance (g_m, given in symbols), indicating that the origin of photoresponse is dominantly due to photogating effect and not only due to photoconduction (see equation (4)). R is 6 A W^{-1} at a low optical power of 1 nW which is two orders of magnitude larger as compared to the previous work. In other 2D materials like InSe, photogating occurs in a similar manner through traps centres located at defect states, SiO_2-In_2Se_3 interface and surface-absorbed molecules [9, 103]. Holes from the photogenerated carriers in In_2Se_3 get trapped in these states, which increases the recombination lifetime. the Photocurrent is strongly dependent on the back-gate voltage (V_g) and can be modulated from 6.9 A W^{-1} to 157 A W^{-1} as V_g is swept from −60 V to 70 V. By changing the V_g, the photodetection mechanism can be tuned from photoconduction (in OFF state) to photogating (in ON state). Responsivity monotonically decreases with increasing illumination intensity due to saturation of trap states which is also observed in 10 nm thick BP [104]. Potential inhomogeneity due to a random distribution of trapped charges at interfaces, vacancies, dislocations, or grain boundaries in BP act as the trap centers for charge carriers. Additionally, it has a broad detection range upto mid-IR and a 3 dB cut off of 10 kHz (which originates due to PV effect). BP photodetector is capable of resolving incident light polarization due to an asymmetric band structure that causes anisotropy in electronic and optical conductivity.

Artificial hybrid heterostructures provide a suitable platform for the manifestation of the photogating effect. The intrinsic photo responsivity of Gr is limited by its weak light-matter interaction and small carrier lifetime. Gr-semiconductor nanohybrids are explored in this context where excellent light absorption properties of low dimensional semiconductors are combined with the high carrier mobility of Gr. The Electric field at the interface of the heterostructure facilitates charge separation. Charge carriers that get trapped in the semiconductor act as a local gate that modulates the carrier density and hence the conductance of the Gr channel. Colloidal PbS Q-dots when coupled with Gr show ultra-high photoresponse. Q-dots are strongly

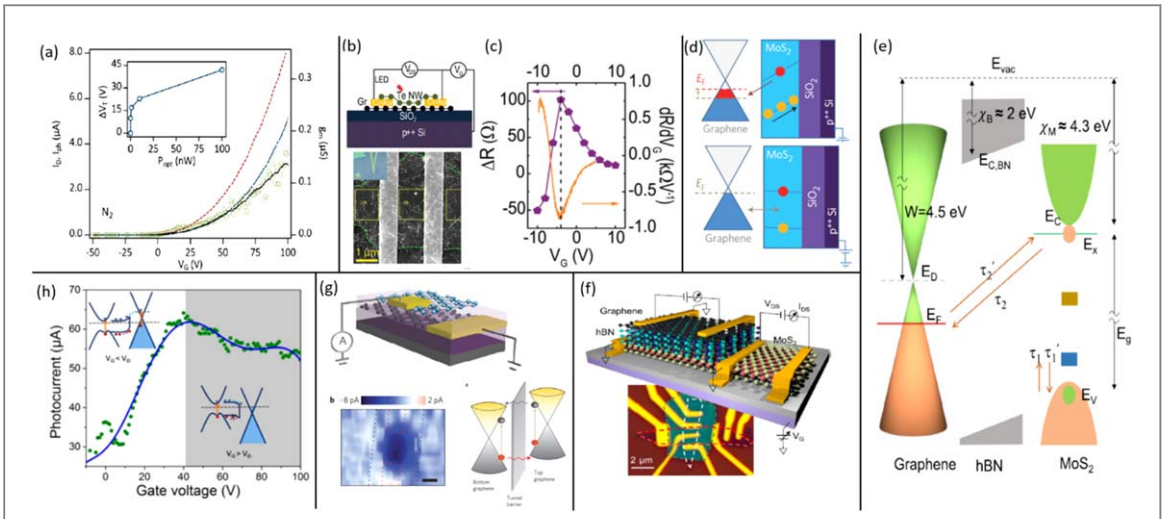

Figure 4. Photogating in 2D materials and hybrids. (a) Transconductance (green open symbols) in a monolayer MoS_2 phototransistor [62]. The right y-axis gives the source-drain current (I_{DS}) in light (red) and dark (blue) conditions. (b, c) Photogating in a Gr-Te NW hybrid. The device schematic with circuit diagram is given along with an optical micrograph of the device [16]. (c) The change in resistance ΔR due to illumination as a function of V_g, which follows the dR/dV_g curve [16]. (d) Schematic of charge transfer process in a Gr-MoS_2 hybrid. Red and yellow circles represent electrons and holes in the conduction and valence bands of MoS_2, respectively [33]. (e) Schematic of the band alignments Gr/hBN/MoS_2 showing the different trap states and excitonic energy levels along with charge transfer directions [105]. (f) Schematic with circuit diagram of a vdW heterostructure using hBN as a spacer layer in between Gr and MoS_2 [105]. (g) Schematic of graphene double-layer heterostructure with a thin tunnel barrier. Schematic of photoexcited hot carrier transport under illumination. The lateral arrows represent tunnelling of hot electrons (grey) and hole (red) across the tunnel barrier. A scanning photocurrent image of the heterostructures at an excitation wavelength of 900 nm [106]. (h) Photocurrent as a function of gate voltage in Gr-Bi_2Te_3 hybrid. Insets show the energy band diagram where blue dots are photogenerated electrons, while red hollow dots are holes [107].

light-absorbing with wavelength tunability in PbS Q-dots from 500 nm to 2100 nm [15]. During the formation of the hybrid, electrons from Gr are transferred to the Q-dot layer, forming a built-in field, equilibrating the Fermi levels. Upon illumination, band bending at the interface favours the flow of holes from Q-dots to Gr, which changes the Gr resistance, while oppositely charged carriers remain trapped in the Q-dot layer as shown schematically in figure 1(e). The gating effect of electrons ensures that the holes are recirculated in the Gr channel in between the source and drain electrodes, leading to a large photogain in the system. The photoresponse is of the order of 10^7 A W^{-1} but with a rise time of 10 ms. Application of a positive gate voltage, that reduces the potential barrier, can expel electrons in the Q-dot to Gr and reset the system. A Similar effect of band bending leading to photogating has also been observed in Gr coupled to NWs [16]. Figure 4(b) shows the schematic and optical image of the Gr-Te NW hybrid photodetector. In the hybrid, there is band bending as electrons flow from the NW to Gr depending on their respective work functions due to the interfacial potential drop. This prevents the electron flow indefinitely to Gr. In the $R - V_g$ under illumination, at $V_g - V_d$ (Dirac point potential) < 0, R decreases as holes from Te NWs flow to Gr. While at $V_g - V_d > 0$, the holes reduce the channel conductance and R increases. Figure 4(c) shows that $\Delta R \propto dR/dV_g$, that establishes the photogating effect. It exhibits a maximum photoresponsivity of $\sim 10^6$ A W^{-1} at 175 K in the NIR regime (920 nm–1720 nm). Roy *et al* [33, 108] demonstrated ultra-high photoresponse of 10^{10} A W^{-1} at low temperature in Gr-MoS_2 heterostructure. MoS_2 acts as the light absorbing layer, while Gr efficiently helps in carrier transport. A schematic of the charge exchange process is given in figure 4(d). Intensive studies on Gr/TMDC hybrids were also performed to understand the charge transfer mechanisms at the interface [105, 109–111]. Ahmed *et al*, [105] studied the influence of traps states on photoresponse by introducing a spacer layer of hBN (see figure 4(f)). The charge trapping mediated slow dynamics in the Gr/hBN/MoS_2 photodetector gives rise to a fast positive component of photocurrent followed by the usual negative photoresponse. Another interesting observation in this hybrid is a strong negative photoresponse at infrared wavelengths (up to 1720 nm), which is much lower than the band gap of a single layer MoS_2 [105]. This has been attributed to defects/traps in MoS_2 lying between conduction band level and excitonic (E_X) levels (see the schematic of figure 4(e)) since control samples of Gr/hBN show no NIR response. Using a similar model, Khasid *et al* [112] showed through time-dependent photo relaxation measurements, resonant quantum tunnelling occurs from E_X of a TMDC to E_F of Gr in Gr/MoS_2 hybrids.

High responsivity, broadband photodetection has been achieved in a variety of other graphene-based vdW hybrids in which photogating plays a major role. For example, Liu *et al* utilized a Gr double-layer heterostructured photodetector (see figure 4(g)) with a thin tunnel barrier of dielectric Ta_2O_5 to obtain a large photoresponse (responsivity $\sim 10^3$ A W^{-1}) at room temperature [106]. In this unique structure, hot electrons

and holes are separated by selective quantum tunnelling that reduces carrier recombination. Upon optical illumination, photoexcited hot carriers tunnel from the top graphene layer to the bottom layer. This results in a strong photogating effect from the charge build-up on the top layer onto the bottom Gr channel as shown in the schematic of figure 4(g). Bi_2Te_3 nanoflakes grown on Gr shows a responsivity of 37 A W^{-1} in the NIR wavelength of 1550 nm [107]. The magnitude of photocurrent as a function of gate voltage is determined by the strength of the built-in electric field at the heterostructure interface, which is an atomic gapless interface, due to the direct epitaxial growth of the nanocrystals on Gr. The direction of the built-in electric field is switched across the Gr Dirac point and hence the photocurrent polarity remains the same throughout the gate sweep interval as demonstrated through figure 4(h). In a recent work by Zhao *et al* Gr/SnS_2 vdW heterostructure showed appreciable photoresponse in the broadband range of 365 nm to 2240 nm [113]. They demonstrate through simulations that separation of charges and photocarrier generation can be effectively tuned by an external electric field through the photogating effect from trapped carriers at the interface. Experimentally, they tune the barrier height and width of Gr-SnS_2 interface. This work demonstrates that by employing Fowler-Nordheim tunneling model, Poisson equation and drift-diffusion simulations, carrier trapping at vdW interfaces can be well understood.

4. Material and device engineering to enhance photoresponse

4.1. Coupling with metallic nanoparticles

Plasmons are the collective oscillations of an electron liquid in metals and semiconductors. Plasmon-assisted photodetection in 2D hybrid structures can be achieved by local electromagnetic (EM) field enhancement using metallic nanostructures or through plasmonic waveguide field enhancement. When the frequency of collective charge density of metallic nanostructures matches that of the incident light, there is a resonance of local surface plasmons (LSPR) [114]. This results in an intense local EM field in the vicinity of the nanostructures. The 'near field' due to LSPR, is quantified by the integrated near field enhancement given by $(|E|/|E_0|)^2$. The confinement of the EM field can be changed by changing the size and shape of the metal nanoparticles. In figure 1(c), the EM field at the junction of two Ag nanoparticles kept 0.34 nm apart is enhanced up to 10^6 times enhancement [30, 31].

Light trapped around the surface of the nanoparticle leads to strong light–matter interactions in Gr and other 2D materials. Sensitization by metallic nanoparticles, allows the photoresponse to be enhanced as well as engineered for a specific spectral range. Responsivity of 2 A W^{-1} was observed through plasmonic coupling of Gr with metal nanoparticle dimers [31]. The photodetector was designed such that a CVD grown Gr layer lies in between two layers of Ag nanoparticles. The electric field shows a huge enhancement for a gap of 0.34 nm. It decreases as the distance d between the two Ag nanospheres increases. Photodetection in the Gr/silver-nanoparticle hybrid arises from a combination of photovoltaic, photo-thermoelectric or bolometric processes which work in tandem and the highest responsivity obtained was 3.2 A W^{-1} between 330 nm and 450 nm. Interestingly, a responsivity of 14.5 A W^{-1} was observed at 280 nm [31]. This is due to large DoS around the M-point of the Brillouin zone of Gr, and is also aided by the strong disorder induced in Gr through ruptures arising from the transfer process which gives rise to a large number of potential traps. A response of ~2.2 mA W^{-1} was achieved in Gr with plasmonic gold nanostructures around 530 nm (extinction peak of Gr—nanoparticle conjugate) [37]. Additionally, these nanostructures can be designed to resonate at a particular wavelength and can be used for selective wavelength amplification. Fang *et al* [115] showed that if a plasmonic antenna (array of Au heptamers) is sandwiched between two monolayers of Gr, the photocurrent increases by 800% due to excitation of tunable Fano resonances. Apart from enhancement of electric field due to plasmonic structures that increase absorption in Gr, hot electrons created in the gold structure transfer charge to Gr, which increases the photoresponse.

Echtermeyer *et al* [12] showed that when plasmonic nanostructures were placed near the Gr/metal junction, photovoltage increased by a factor of twenty. The metal nanostructures were designed to produce strong light absorption in the visible range and were fabricated close to contacts as shown in figure 5(a) so as to guide the incident EM energy directly to the p–n junction region. The photovoltage distribution near the contacts is shown in a colour plot in figure 5(a). The Au nanoparticles act as a nanoantenna which enhances optical absorption as well as act as a subwavelength scattering source that assists in the enhancement of photocurrent. Lin *et al* [13] reported larger absorption of light by MoS_2 flake in presence of gold nanoparticles attributing to field enhancement due to surface plasmons at $\lambda = 514$ nm. In their work, enhancement in photocurrent was seen for wavelengths up to 660 nm and the cut off wavelength is determined by the size of Au nanoparticles. Similar work was reported in MoS_2 by Hu *et al* [116] in which Au nanoparticles were deposited on MoS_2 resulting in an increase of photoresponse.

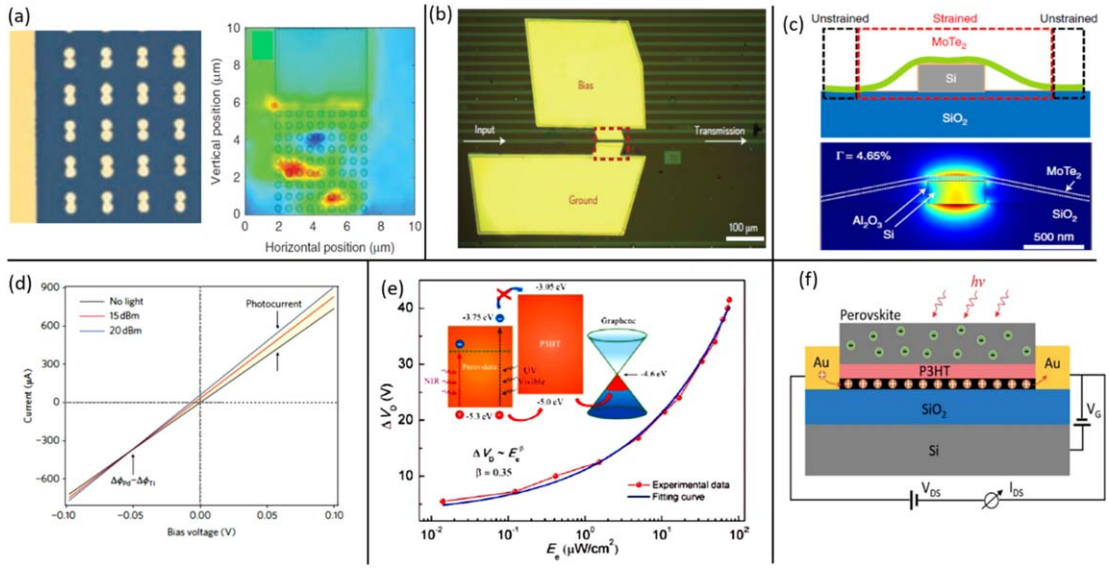

Figure 5. Description of photodetectors that are aided by photo-enhancement mechanism through plasmonic coupling, integration with waveguides, and coupling with organic materials. (a) SEM image of the Gr devices with plasmonic nanostructures near the contacts [12]. Photovoltage maps of a device with color scale is from -4 μV (blue) to 12 μV(red). (b) Optical microscope image of a bilayer Gr coupled to a Si waveguide, with two Ti/Au paddles [29]. (c) Schematic of a $MoTe_2$ crystal on Si ring photonic cavity with a Si bus waveguide [17]. Color map shows a strong localized strain on the $MoTe_2$ lying on top of the waveguide. (d) Photocurrent in contact engineered Gr with inter-digitated asymmetric metal electrodes [38]. (e), (f) Photodetection in organic/2D hybrids. Device schematic of perovskite/P3HT/Gr phototransistors. Graph shows shift in Dirac point with illumination intensity with inset showing the charge transfer mechanism is given alongside [24].

4.2. Coupling with organic materials

Successful development of thin film organic photodetectors (OPDs) faces major challenges such as short exciton diffusion lengths (of the order of few nanometers), low carrier mobility and poor photoresponse beyond NIR wavelengths [117, 118]. Studies have demonstrated improved photosensitivity and high detector gain by integrating organic compounds with 2D vdW materials [119]. Here, the organic semiconductor acts as a tunable bandgap photoactive material, and the vdW material is used as a high-quality substrate with high mobility and an ideal interface for fast charge carrier transportation. In most cases, 2D materials can effectively collect the injection exciton (from organic material) thereby enhancing the electronic performance. For instance, Poly-3-hexylthiophene (P3HT) [24], Methylammonium Pb Iodide (MAPI) [25], Dioctyl-benzothieno-benzothiophene (C8-BTBT) [120], when combined with Gr show ultrahigh gain. 2D perovskite crystals of an organic Pb halide compound with Gr electrodes show a high response of 2100 A W^{-1} [8]. The inorganic component, Pb, with d orbitals has a large DoS, while the organic component has mechanical strength and structural flexibility. Perovskite/P3HT/Gr multi-heterojunction phototransistors (device schematic is given in figure 5(e)) show responsivity of 4.3×10^9 A W^{-1} [24]. Here, photons are absorbed by the perovskite layer while P3HT layer helps in the separation of electron and holes which gets injected into Gr. The shift of Dirac point in Gr due to charge transfer is shown in figure 5(f) with inset demonstrating the band energy alignment. Photodetectors made from $CsPbBr_{3-x}I_x$ nanocrystals grown on bilayer Gr in FET configuration shows a high responsivity of 8.2×10^8 A W^{-1} [25]. It shows a slow response time ~1 s attributed to the resistance to carrier transport from the nanocrystal to Gr because of a potential energy barrier. When integrated with Gr, C8-BTBT shows a responsivity of 1.57×10^4 A W^{-1}, with a response time of ~25 ms [120]. The gate dependence follows dR/dV_g curves, which is a signature of photogating. However, C60/pentacene integrated with Gr phototransistor shows spectral response from 405 nm to 1550 nm with a high gain of 5.2×10^5 and a fast response time of ~275 μs [121]. Apart from Gr, MoS_2 has also been explored in conjugation with organic materials that demonstrate excellent optoelectronic properties [122]. Heterostructures of fullerene (C_{60}) with MoS_2 shows excellent photovoltaic properties, with the short-circuit current increasing by five times as compared to pristine MoS_2 [123]. The absorbance of MoS_2 increases by 1% due to a change in the surrounding refractive index brought about by an array of C_{60} molecules. MoS_2 and poly(vinylidene fluoride-trifluoroethylene) (P(VDF-TrFE)) heterostructure shows a wide spectrum photo response from ultraviolet (375 nm) to long infrared wavelengths (10 μm) by utilizing multiple mechanisms i.e., pyroelectricity, ferroelectricity, and photoconductivity [124]. Lim *et al* [125] showed that p-n junction formed by pentacene and MoS_2 shows the lifetime of the charge-separated state (that directly affects the efficiency of charge separation) to be 5.1 ns, which is much longer than the TMDC inorganic heterostructures.

4.3. Integration with photonic platforms

Gr-based hybrid photodetectors improvs responsivity by orders of magnitude but at the cost of quick response speed and reduced spectral range. Integration with photonic platforms has recently made it possible to maintain the high speed and spectral bandwidth. The electric field distribution of transverse electric mode in a Si channel waveguide increases manifold times [61]. Intergrating Gr to a cavity/waveguide structure enhances light absorption through coupling by an evanescent field [29, 36], leading to optical absorption and the generation of photocarriers as shown in figure 1(b).

In 2013, a Gr photodetector evanescently coupled with waveguide showed a responsivity of 0.1 A W^{-1} with a bandwidth of 20 GHz shown in figure 5(b) [29]. Wang *et al* [19] reported a Gr-Si based photodiode produced by integrating Gr onto silicon-on-insulator with response in NIR up to 2.75 μm with a responsivity of 0.13 A W^{-1} at a bias of 1.5 V at room temperature. Following these, improved device architectures were adopted for achieving higher responsivity and bandwidth by using hBN encapsulation [126], creating a p-n junction [99], and plasmonic excitations [127]. Recently, Guo *et al* reported a Gr photodetector based on bolometric and photoconductive effects integrated with Si waveguide with a response of 0.4 A W^{-1} at 0.3 V bias working at 1.55 μm and above, with a 3 dB bandwidth of 40 GHz. TMDCs like $MoTe_2$ have also been integrated with a silicon micro-ring resonator and shows a response of 0.467 A W^{-1} at 1550 nm, arising from mechanical strain, with a bandwidth of 35 MHz [17] (see figure 5(c)). Heterostructures such as Gr-$MoTe_2$ hybrids have also been integrated on a silicon photonics platform [35] (see figure 1(h) for device schematic). It shows a high measured bandwidth of at least 24 GHz and is a result of several factors that work in tandem in these structures. The state of art photodetector is a plasmonic integrated hybrid structure that includes a Gr photodetector coupled with arrayed bow-tie shaped nanostructure to excite surface plasmon polaritons. It has a responsivity of 0.5 A W^{-1} with a bandwidth of at least 110 GHz and responds from 1480 to 1620 nm [11]. Thus, integrating 2D heterostructures with Si photonic platforms provides an ideal system to realize high-performance, high-speed photodetectors. In table 1, we show the performance of waveguide coupled 2D materials and hybrids.

5. Outlook

The photodetection performance of vdW materials and heterostructures has significantly improved in the past decade by coupling other photoactive nanomaterials and through materials engineering. Considerable efforts have been made to achieve low dark current, high external quantum efficiency, low noise, high gain, responsivity and detectivity, particularly by optimizing device architecture, growth and placement of nanomaterials, interface coupling, contact engineering and through understanding the fundamental physical and chemical properties of hybrid vdW heterostructures. In the following section, we provide a short summary of this field in terms of responsivity and bandwidth, and photodetector operation of spectral regime.

5.1. Photodetector performance of 2D materials and hybrids

Different types of vdW structures can form heterojunctions with each other or with other nanomaterials, without the need for close lattice matching [130, 131]. Photodetectors based on PV and PC effects have demonstrated exceptional performance in terms of responsivity, response speed and noise level in the UV-NIR wavelength regime. However, for wavelengths in terahertz (THz) region, photo-thermoelectric and bolometric effect based on temperature-difference-driven voltage becomes the dominant photodetection mechanism [69, 132–134]. Interestingly, metal electrodes to Gr micro-ribbon arrays spaced at a distance shorter than the free space wavelength, resulting in resonant plasmonic coupling. This enhances the absorption and increases the efficiency of THz detection [134]. In the microwave frequency range of 1−5 GHz, photocurrent induced in a suspended monolayer Gr by differentially gating both sides of the layer, leads to PTE based microwave detection [135]. Graphene-based Josephson junction bolometers show a fast thermal relaxation ~17 ps operating at 3 GHz [136]. Recent studies on Gr-Josephson junction bolometer shows a NEP of 7×10^{-19} W $Hz^{-1/2}$, limited only by intrinsic thermal fluctuations [137]. The superconducting-Gr-superconducting junction is coupled to an on-chip LC oscillator. On absorbing radiation, the resonance frequency changes, which serves as a thermometer. The detector has a low NEP of 30 zW $Hz^{-1/2}$ and a thermal time constant of 500 ns [138]. These types of detectors show promise for thermal detection towards the single-microwave photon regime.

In figure 6, we show the responsivity as a function of bandwidth in 2D materials and their hybrids. Amongst individual 2D materials, bare Gr has the highest bandwidth but a low responsivity of few mA W^{-1}, while TMDCs show higher response, of few mA W^{-1} to few A W^{-1} (after contact engineering and other photoresponse enhancement techniques) and detection speeds of up to 10 MHz. For example, MoS_2, on interfacing with a layered perovskite film shows a high responsivity exceeding 10^4 A W^{-1} and specific detectivity ~10^{14} Jones (cm$Hz^{1/2}$ W^{-1}) [139]. The perovskite layer edges are in contact with the surface of MoS_2 and electrons flow from MoS_2 to the perovskite, resulting in a type-II band alignment and a suppressed dark current.

Table 1. Photodetector parameters for waveguide coupled 2D materials.

Material	Waveguide type	Responsivity	Bandwidth	Wavelength of operation	Bias	Year	References #
Gr	SOI bus waveguide	0.1 A W^{-1}	20 GHz	1450–1590 nm	0	2013	[29]
Gr p-n junction	Si slot waveguide	35 mA W^{-1}	65 GHz	1560 nm	0	2016	[99]
Bilayer Gr plasmonic hybrid	Si photonic waveguide	0.5 A W^{-1}	110 GHz	1550 nm	0.6 V	2019	[127]
Gr monolayer sandwiching SiN membrane	SOI waveguide	3.5 V W^{-1}	65 GHz	1550 nm	0	2021	[128]
Black Phosphorous	Si photonic waveguide	19 mA W^{-1}	3 GHz	1570–1580 nm	−0.4 V	2014	[129]
strained $MoTe_2$	Si micro-ring resonator	0.5 A W^{-1}	0.035 GHz	1550 nm	−1 V	2020	[17]
$MoTe_2$-Gr vertical hybrid	planar Si photonic waveguides	0.2 A W^{-1}	24 GHz	1300 nm	−3 V	2020	[35]

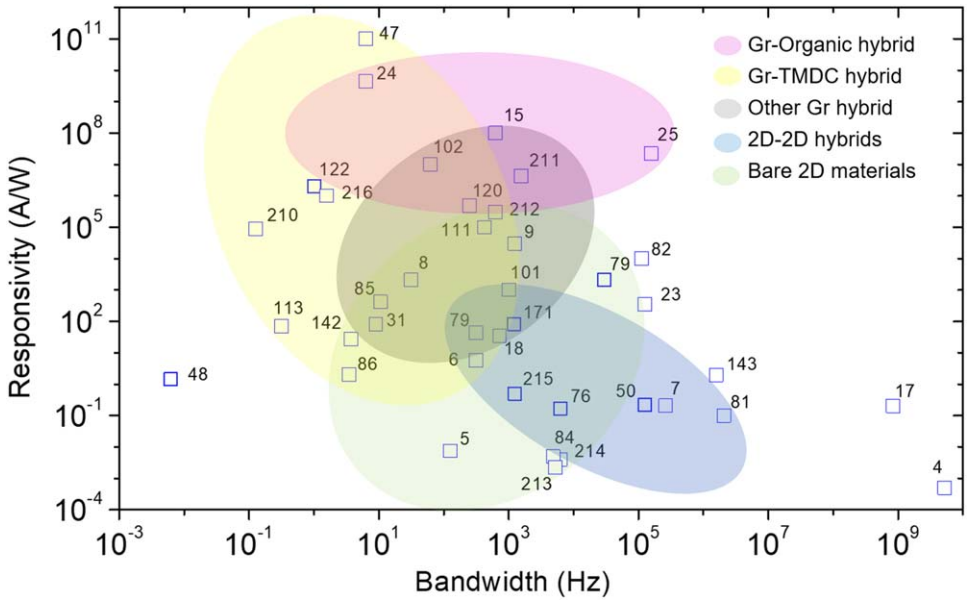

Figure 6. Responsivity as a function of bandwidth in 2D photodetectors. The shaded ellipses show a cluster of the following type of structures: Gr-organic hybrids, Gr-TMDC hybrids, other Gr hybrids, 2D-2D heterostructures and pristine 2D materials. The number next to each data point represents the corresponding reference.

Upon irradiation, electron transfer occurs from perovskite layer edges to MoS_2 while the holes are trapped in the perovskite crystallites. The fabrication procedure is simple and involves spin-coating the perovskite layer on the CVD grown MoS_2 [140]. Other 2D analogues like InSe [9, 141, 142], and Bi_2Se_3 [143] also show a similar trend, and their spectral bandwidth is much larger, extending into the NIR region. Few layered InSe nanosheets show a photoresponse from 10–30 A W^{-1} (wavelength dependent, from ultraviolet to near-infrared) [141, 142]. Feng *et al* observed an ultrahigh responsivity of $\sim 10^4$ A W^{-1} with 5 ms response in InSe nanosheets of thickness 30 nm (where the response is maximum) originating from multiple reflection interference at the air/InSe/SiO_2/Si interface [9]. The blue shaded region in figure 6 shows 2D-2D heterostructures that form a p-n junction and type II band alignment. These hybrids show photoresponse much greater than 10 A W^{-1} with an improved bandwidth due to the presence of the built-in field that leads to quick charge separation. Since these materials have a mobility that is much less than Gr, 3 dB bandwidth is still limited to the MHz range. Integrating graphene with 2D materials, nanowires and Q-dots have shown remarkable effects, as summarized in figure 6. We observe two main features from this graph; while individual materials engineered can show appreciable photoresponse properties, combining with other vdW materials have paved the way for single photon detection [50] and high-rate in excess of 105 Gbit/s binary transmission of a non-return-to-zero data stream [128]. In general, there is either a very large bandwidth (>GHz), relevant for data communication applications using 2D materials integrated with Si photonic platforms, or of very high responsivity using Gr based hybrids, relevant for imaging and sensing applications [144].

If we observe the spectral regimes of photodetection in 2D materials, the operation regime of the individual materials can be exploited when integrated with Gr to produce high performance photodetectors as illustrated in figures 6 and 7. Gr/Si Q-dots show a responsivity of 10 A W^{-1} in MIR (~4000 nm) and 10^9 A W^{-1} in UV region (375 nm) [14] Si Q-dots, when doped with boron, shows LSPR at 3 μm while conventional band-to-band transitions based on optical absorption by the Q-dots occur in UV-Visible region. Combining with NWs like Te which can have a tuned bandgap of 0.65 eV, results in NIR response [16]. Responsivity as a result of photogating effect is 10^6 A W^{-1} and the temperature operating range is 220–260 K. Using Bi_2Te_3 nanocrystals (which have a small band gap) in tandem with Gr shows NIR response [107]. There is effective charge transfer at the interface and separation of photoexcited charge carriers resulting in a photocurrent up to 170 μA and a rise time of 8.7 ms. Interestingly, twisted bilayer Gr (TBLG) at 1.81^0 angle shows photoresponse in MIR region [145]. The excitation of electrons from filled moiré bands to empty moiré bands shows absorption exceeding 4.6% due to enhanced DoS close to the top of filled moiré bands and bottom of empty moiré bands. Currently, moiré excitons of TMDCs which are created by a long-range periodic potential in an artificial superlattice have attracted significant research interest for optical and optoelectronic functionalities. These excitons are spatially present in two different layers and may be confined by the moiré potential, giving rise to localized excitonic states [146, 147]. The excitonic energy levels are much lower than the neutral excitons of the corresponding layers while the energy level difference between any two moiré excitonic states is 22 $\pm$ 2 meV [147]. Moiré excitons

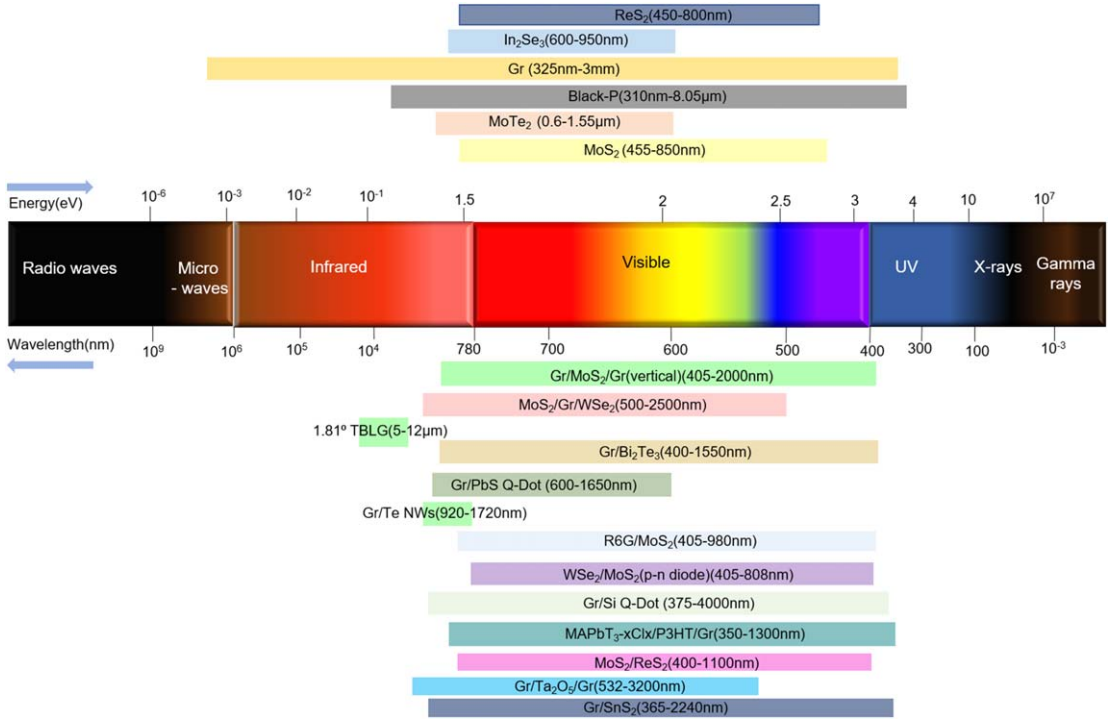

Figure 7. Wavelength regimes of operation in individual 2D material photodetectors (top) and their hybrids (bottom).

have potential applications as a regular array of Q-dots as single photon emitters [148] and also show photon antibunching properties [149]. In the long-wave IR regime, PtSe photoconductors on TiO_2/Au optical cavity shows a quick photoresponse time of 54 ns with a responsivity of 54 mA W^{-1} and operates upto 8.35 μm [150]. Graphene/HgCdTe heterostructure infrared photodetectors shows responsivity of 2.60 A W^{-1} working upto mid-infrared wavelength region of 5.2 μm [151]. The state-of-the-art research in HgCdTe alloys has shown enhancement in MIR photoresponse as well as detectivity by integrating monolithically with meta lenses [152]. Ge/perovskite heterostructure photodetector, operating at 1550 nm shows responsivity of 1.4 A W^{-1} at a low bias of 1 V. The perovskite coating gives the lowest reflection at 1550 nm wavelength and along with type 1 band alignment, aids charge transport from perovskite to Ge [153].

5.2. Future, challenges and new aspects

vdW heterostructures have been actively explored for their high performance photodetection in a wide range of the electromagnetic spectrum. In the previous sections, we have discussed how device engineering and fundamental understanding of the physical mechanism plays a critical role in enhancing device performance. However, there are several challenges that need to be addressed such as room temperature photodetection in a broad wavelength regime, mass production of vdW materials, standardizing measurement protocols, better methods to optimize dark current and increase the signal-to-noise ratio, etc. Thus, a clear understanding of the different factors that can affect the long-term performance of a photodetector would be essential to carry forward the field of vdW heterostructure-based photodetectors to a technologically viable platform. Below, we discuss key challenges as well as our perspective on future research directions to enhance and explore the unique characteristics of vdW hybrids.

5.2.1. Selection of correct design strategies for vdW hybrids to enhance device performance

Different device types such as photodiode, photoconductor or phototransistor have exploited the low dimensionality of vdW heterostructures as discussed in previous sections. For example, in a photodiode device geometry, the photodetector efficiency depends on how well the built-in field can separate the charge carriers. This further depends on the type of device architecture used, whether it is vertical or horizontal [154]. In addition, another interesting aspect of improving the photodetection efficiency involves integration of FET with organic photodiode modules on the same substrate to achieve low dark current density [155].

5.2.2. Fundamental understanding of the physical mechanism behind photodetection

There have been many reports on different photophysical mechanisms like photogating, photoconduction, bolometric response etc to understand charge transfer and transport in 2D materials. However, not much literature is available that describes the energy transfer (ET) and charge transfer (CT) mechanisms in hybrids. In type II aligned hetero-bilayers of TMDC, PL quenching has been observed. Low temperature PL studies on $MoSe_2/WS_2$ show that the intensity of $MoSe_2$ A exciton is enhanced in resonance with A, B, and C absorption peaks of WS_2 [156]. This effect should originate from photodoping that influences the emission intensity due to charge transfer. But, the exciton-trion ratio of $MoSe_2$ is constant across the B exciton resonance of WS_2, proving that the intensity enhancement cannot be attributed to changes in carrier densities and thus can arise from ET. These type of heterostructures show Förster type of ET with ET rates of ~1 ps. In Gr/TMDC hybrids there have been some revelations regarding near-field interlayer ET. A coupled Gr/ $MoSe_2$ heterostructure shows PL quenching by three orders of magnitude as compared to bare TMDC [157]. Moreover, bare $MoSe_2$ displays an exponential decay with exciton lifetime of ~1 ns and the heterostructures shows a faster lifetime of <20 ps. PL intensity of the A exciton (normalized by photon flux) is observed to reduce with photon flux in bare $MoSe_2$ due to highly efficient exciton-exciton annihilation (EEA). It is constant in the Gr/ $MoSe_2$ heterostructure which suggests an efficient relaxation pathway for excitons possibly through ET. Froehlicher *et al* suggest that there is an opening up of a non-radiative decay channel which reduces the A exciton lifetime as well as bypasses EEA. ET being a faster process and presence of large in-plane dipoles in monolayer TMDCs favors Förster energy transfer to Gr. Zhen Xu *et al* have utilized differential reflectance pump probe spectroscopy measurements to study the interlayer transfer of electrons from TMDC to Gr [158]. Upon excitation, hot electrons are transferred to MoS_2 from Gr following which electrons thermalize and cool within a time scale of a few picoseconds. Their observations indicate that the interlayer transfer process is dominated by strongly localized disorder states in the TMDC layer.

Typically, the photodetection mechanism in organic- 2D hybrid photodetectors is dominated by traps that usually capture one type of carrier and result in a large internal gain due to photovoltaic, photoconductive or photogating effects [159–161]. However, there is still not much clarity about the exact charge transport mechanism occurring in hybrid organic/2D vdW heterostructure system. Thus, a more comprehensive and clear understanding of the photophysics, interface engineering between organic and 2D vdW heterojunction, morphology regulation of organic semiconductor and device scaling is required for the realization of high-performance photodetectors. It is noteworthy that the selection of organic- 2D heterostructures can be further extended to the large library of photoactive organic semiconductors based on their intrinsic properties with suitable energy level matching leading to better charge transportation occurring at the interface. This could lead to new avenues towards fast and high performance 2D- hybrid practical photodetectors.

5.2.3. Noise reduction and standardization of characterization

The performance of a detector should be reported as a function of electrical bandwidth, temperature, and optical wavelength with the figures of merit of quantum efficiency, responsivity and the noise current (I_n). The noise in a photodetector limits its sensitivity by limiting the minimum incident power that a detector can detect. The specific detectivity (D^*) which is inversely proportional to the noise current is given by [56],

$$D^* = \sqrt{AD_f}\mathscr{R}/I_n \tag{7}$$

where A is the effective area of the detector in cm^2, D_f is the electrical detection bandwidth in Hz which can be calculated directly from the integration time constant (τ_c), where $D_f = 1/2\tau_c$ and $\mathscr{R}$ is the responsivity in $A\,W^{-1}$. Further, noise estimation has become the most neglected performance aspect in nanomaterial-based photodetectors, that can result in the overestimation of detectivity value by several orders of magnitude [162]. It is often assumed that detector noise is solely dominated by white noise. Typically, the e-h pair generation process involves three types of noise i.e., shot noise, Johnson noise and flicker or $1/f$ noise. Thus, it becomes essential to analyse the origin of noise in photodetectors by area scaling based on the dominant component of the noise to accurately calculate the noise current. This would avoid unreliable detectivity values and facilitate true performance comparison. A more reliable way to estimate the noise characteristics is to measure the noise power spectrum of the detector, as explained elsewhere [163]. The shape of the power spectra and the exponent depends on the time- scales of the physical mechanism that is responsible for the fluctuations, and can provide crucial information about the underlying defect dynamics in a system.

Noise can be reduced by designing an appropriate device architecture. Gr–metal interface shows current crowding with charge transfer length of 0.1–1 μm. Large contact noise of $1/f$ nature in Gr arises from mobility fluctuations (due to potential fluctuations in the SiO_2 substrate) in the charge transfer region underneath the metal contacts. Invasive contacts also lead to large noise component as they extend into the current flow path. Separation of SiO_2 from Gr by using hBN improves the noise in a device [164]. Noise in Gr photodetectors in FET configuration comes from channel noise and metal-Gr contact noise. Noise in edge-contacted Gr can be

decreased by keeping the separation between contacts that form the channel greater than or equal to 1.2 μm as shown by Kakkar *et al* [165] Inclusion of a graphite gate electrode to the encapsulated Gr device with an addition of few-layer MoS_2 in between Gr and hBN shows a record low value of noise (area normalized power spectral density of 5.2×10^{-9} μm^2 Hz^{-1} at 1 Hz) in a Gr field-effect transistor [165].

5.2.4. Reduction of dark current in hybrid 2D photodetectors

2D hybrid heterostructures have the ability to reduce the dark current, which is otherwise a limiting factor to obtain high detectivity. By stacking monolayer WS_2 between two sheets $MoTe_2$, Tenghui Ouyang *et al* [166] demonstrates suppression of dark current to 90 pA. In this manner, the avalanche photodiode is configured as two back-to-back Schottky barriers formed at WS_2-$MoTe_2$ heterojunctions which assist in reducing the dark current and their device exhibits detectivity limits of 10^9 Jones. Capping a 2D halide perovskite on MoS_2 has also shown suppression of dark current ~10 pA leading to detectivity of the order of 10^{13} Jones [167]. In this heterostructure, the interlayer charge transfer from MoS_2 to 2D halide leads to six-fold reduction in the dark current value compared to pristine MoS_2. Apart from acting as an electron reservoir reducing the free carrier concentration, the 2D halides also helps= in passivating surface defects on MoS_2 leading to fast response times of the order of 4 ms. Dark current in TMDCs can also be significantly reduced by decorating with photo-sensitive materials, such as quantum dots, which also helps in increasing the responsivity. Pak *et al* [168] reported that p-type-MnO decorated on n-type MoS_2 form an ideal p-n junction with a low dark current value. The quantum dots block electrons that help in reducing the dark current and hence help to improve detectivity limits.

5.2.5. Room temperature photodetection

Commercially available 3D photodetectors work at room temperature (RT) in the visible (Si detector) and NIR (InGaAs, Ge detector) spectrum. Si photodetectors have a responsivity of <1 A W^{-1} and Specific Detectivity $\sim10^{12}$ Jones. Infrared photodetectors are limited from widespread usage specifically due to the need for cooling to cryogenic temperatures [169]. High-performance photodetectors operating at RT thus have a huge demand in practical applications. Gr photodetectors work in the MIR and THz region by PTE mechanism and plasma-wave assisted mechanism [56]. These detectors are operational at RT with very low *NEP* ~0.1–1 nW $Hz^{-1/2}$ [132, 170]. Waveguide integrated photodetectors coupled to Gr and Gr hybrids are operational in the NIR region at RT and show ultrafast photoresponse [17, 35]. Other 2D materials like BP and Te which have tuneable band gaps in the MIR region also show commendable photoresponse properties. hBN encapsulated b-As_xP_{1-x} show RT operation within 3.4–7.7 μm [171]. It works in the photoconductive mode, with $R = 190$ mA W^{-1} at 3.4 μm and a 3-dB cut off frequency of 19 GHz. A chalcogenide glass waveguide integrated with Te with a bottom Gr gate reported *NEP* of 0.03 fW $Hz^{-1/2}$ at 3 μm operational wavelength [172]. In the field of 2D detectors operating at IR wavelengths, there is a need for high responsivity detectors and 2D hybrid structures show promising potential. BP/MoS_2 heterostructure, working in the wavelength region of 2.5–3.5 μm has $R =$ 0.9 A W^{-1} and Specific Detectivity $\sim10^{10}$ Jones [173]. Here, the MoS_2 acts as an electrode, which is electron selective while the bottom contact of 170 nm thick Au film also acts as a MIR reflector.

Room temperature 2D photodetectors in the visible region are limited by their low photoresponse and unsatisfactory detectivity since they mostly rely on photoconduction mechanisms and have a high dark current and large thermal noise. Hybrids of Gr and 2D materials show excellent photoresponse (see figure 6) and should be investigated further for RT photoresponse. Gr-MoS_2 hybrid shows ultrahigh photoresponse of 10^8 A W^{-1} at RT in the visible range [51]. In a MoS_2-Gr-WSe_2 heterostructure, photoresponse of 4×10^3 A W^{-1} was achieved with a high detectivity of 10^{12} Jones [85]. The p-n junction creates a large built-in field of $\sim2 \times 10^8$ V m^{-1} leading to spontaneous separation of e-h pair, resulting in a lifetime of 53 μs and a high responsivity. Gr-WSe_2 hybrid, with electrical contacts on the individual materials, shows a high response of 350 A W^{-1} at 1 V bias, a quick rise time of 30 μs and a high detectivity of 10^{13} Jones [85]. It shows rectification behavior and PV effect due to asymmetric contacts. A current research direction would be to focus on RT photoresponse of Gr-TMDC heterostructures since they show ultrahigh responsivity and low noise equivalent power.

5.2.6. Detection of a weak optical signal

There has been recent interest in 2D layered materials for ultra-weak optical signal detection for photon counting applications. In as early as 2013, Roy *et al* [50]demonstrated using a dual-gated hybrid Gr/MoS_2 photodetector with photon-counting ability. Low noise and efficient photogating effect of the hybrid leads to the unique ability for this heterostructure to perform number-resolved photodetection. Conventional single photon detectors like Si avalanche photodiodes, superconducting nanowires etc, which are commercially available, suffer from drawbacks such as single-noise ratio, spectral operational range and photon-number resolving ability and with high demand in the emerging quantum technology field, there is ample room for improvement [174, 175]. Carrier multiplication through avalanche breakdown is a well-established process to

increase the internal gain of a photodetector. Based on avalanche mechanism, 2D materials like InSe [176], BP [177] (in a vertical configuration) have an advantage over bulk 3D semiconductors as they can initiate impact ionization at small biases. 2D heterostructures of InSe/BP [178] showed ballistic avalanche breakdown due to a very short active region leading to a higher gain and external quantum efficiency $\gg 1$, operational in the MIR region. In a recent work by Seo *et al* photoresponsive properties of monolayer MoS_2 transistors were investigated in the breakdown regime [179]. It shows impressive values of 3.4×10^7 A W^{-1} and 4.3×10^{16} Jones for responsivity and detectivity respectively at RT. The regime of operation of the transistor is in the OFF state when the dark current is low, but the applied field is high (~0.29 MV cm^{-1}). A Schottky barrier formed at the metal/MoS_2 junction is used to modulate charge carrier injection occurs across the interface. Under illumination, the photogenerated electrons undergo impact ionization which initiates an avalanche breakdown, resulting in a large photocurrent. This work provides a simple design process and an excellent strategy for high-gain room temperature photodetection. Avalanche photodiodes were fabricated by Sangwan *et al* using layered Bi_2O_2Se semiconductor [180]. It works on the principle of carrier multiplication by impact ionization under reverse bias conditions in the depletion region formed at the metal/semiconductor Schottky junction. The photodiode shows a high responsivity of 3000 A W^{-1} and an appreciable bandwidth 1 GHz. Hence, 2D layered systems provide an emerging technology for weak optical signal detection, and are currently in an early stage of development.

5.2.7. Mass production of high quality 2D materials and hybrids and their long-term device stability

There has been remarkable progress in the production of graphene and other 2D hybrid materials by CVD. Currently, different heterostructures such as Gr/hBN [181, 182], MoS_2/Gr [183], WS_2/MoS_2 [184] etc can be grown by CVD. There are crucial growth parameters such as temperature, substrate, gas flow rate, gas pressure and growth time that govern the precise control of 2D heterostructure formation. A detailed review of the growth of hybrids can be found here [185]. An all-CVD process for synthesizing TMDC/Gr hybrids on Au foil was demonstrated by J. Shi *et al* [183]. The 2D layers are grown at high temperatures under ambient pressure, in a three-zone furnace using a carrier gas (inert gas, usually Ar) for transportation of precursor vapours. The Au foil is a crucial growth element since it prevents any doping from Au to Gr during growth, has a multi-faceted structure, shows catalytic ability and is inert to the precursor material for most TMDCs. The heterostructures grown in this manner shows uniformity and has a clean interface. Other 2D heterostructures such as WS_2-WSe_2, and trinary structures such as WS_2-$MoSe_2$-WSe_2 can be grown by a sequential-growth process, using a reverse flow from the substrate to the source during the switching of growth from one material to another [184]. This prevents the existing monolayer to grow by flushing it out using cold Ar gas. This strategy can be used for the growth of a wide range of heterostructures. Heteroepitaxial growth of TMDC superlattices was shown by Jin *et al* where a monolayer of TMDC is first grown in a preferred crystallographic orientation by metal-organic CVD process. This serves as a template for the growth of the subsequent dissimilar TMDC [186]. Lateral or in-plane growth of 2D materials like WS_2/MoS_2 heterostructures can also be accomplished by a one-step CVD process [187]. The substrate wafer with tungsten powder is kept in the cooler zone of the furnace and acts as the substrate for MoS_2 growth, whose precursor (MoO_3) is placed hot zone. Growth parameters are similar to that of a vertical structure, except that the growth temperature is much lower, at 650 °C instead is 850 °C. Other binary lateral heterostructures can be grown using a similar strategy at controlled temperatures. CVD technique has large flexibility in the growth of 2D heterostructures. The strategy for the growth of these hybrids is well-established now and the quality of the interface, electrical properties of the FETs, PL studies etc, all indicate highly crystalline growth of these heterolayers.

Compared to CVD grown 2D material, physical mechanisms like sonication, shear-mixing, ball-milling, electrochemical exfoliation can cleave van der Waals materials leading to fewer defects and high crystallinity and is a well-established technique. These top-down exfoliation methods lead to a low yield of monolayer flakes and prevent industrial scalability [188]. A recent technique, intermediate-assisted grinding exfoliation, which uses micro-particles as force intermediates show a high yield of ~67% and is promising for industrial-grade mass-production of 2D materials like MoS_2 [189] On another note, a recent work by Indra *et al* discusses mass production of 2D devices fabricated from solution-processed 2D material inks [190]. The authors produced highly concentrated nanosheet dispersions of MoS_2, WS_2 and graphene, which acts as printable ink from which printed photodetectors were fabricated. The responsivity of the TMDCs was three to four orders lower than conventional mechanically exfoliated layers. Nevertheless, the printable 2D devices have low-cost processing and much higher throughput, making them viable for industrial applications. This technique can be extended for more complex device fabrication of 2D heterostructures, such as Gr/TMDC hybrids.

Several approaches have been experimented with, to improve device stability, such as by using hBN as an encapsulation layer. It provides high chemical stability, has a wide bandgap, and could eliminate trap states at the interfaces of 2D material-based devices [171]. However, for potential commercial applications, it is critical to develop a high-yield scalable process for producing high-quality 2D materials, and methods to improve device

stability in ambient conditions. Recently, Sebestian *et al* [191] examined the variation in key characterization parameters of MoS_2 and WS_2 FET transistors. Monolayers of the TMDCs were grown on a 2-inch sapphire substrate and then were wet transferred to Al_2O_3/Pt/TiN/p^{++}Si substrate, where Al_2O_3 act as a gate dielectric and Pt/TiN/p^{++}Si acts as a gate electrode. Transfer characteristics on all the devices (230 MoS_2 FETs and 160 WS_2 FETs) showed similar threshold voltages, ON-OFF ratio, and saturation velocity. The FETs exhibit mobilities of 46 $cm^2\ V^{-1}\ s^{-1}$ and 33 $cm^2\ V^{-1}\ s^{-1}$, for MoS_2 and WS_2 respectively, with ON-OFF ratio ($\sim 10^7$). The semiconductor parameters are much greater than 0.9 nm ultra-thin body Si FETs (6 $cm^2\ V^{-1}\ s^{-1}$). The reproducibility and consistency of the FETs can be attributed to the epitaxial crystalline growth of monolayers. These findings show promise for applications of 2D FETs in very large-scale integration circuit chips.

5.2.8. Integration of 2D materials with silicon

The integration of 2D materials with commercial semiconductor devices such as silicon read-out electronics could potentially lead to further miniaturization and development of next-gen electronics and photonic devices [192]. Gr can be integrated with Si in solar cells, where it replaces the metal electrode and the Gr/n-Si interface creates a space-charge region that aid is carrier separation [193]. An array of 2000 devices were fabricated on a 6-inch Si wafer with Gr transparent top gate [194]. MoS_2 based Si solar cells have also developed in the past decade, where the MoS_2 layer enhances light absorption in Si [195]. Presently, on-chip integrated photodetectors based on 2D materials have progressed immensely and show tremendous potential due to large bandwidth as discussed in section 4.3. Numerous studies such as the ones stated above show that Gr is compatible with Si CMOS technology.

However, there are several practical challenges that need to be overcome for the successful integration of 2D materials. This involves a uniform transfer of wafer sized 2D material onto a conventional integrated circuit without degradation as they are easily prone to mechanical damage during the transfer process. Further, the other underexplored challenge is the direct growth of high-quality single crystal 2D material on silicon devices that would require very high processing temperatures, which is not feasible. Although, CVD can enable large-area synthesis of 2D materials, the usual wet and dry methods of transferring CVD grown 2D materials onto device substrate do not currently meet the high-quality standards set by the semiconductor industry [196–198]. Recently Kim *et al* [199] have demonstrated the damage free transfer of graphene and MoS_2 by minimizing the instability-induced damage mechanism using optimal thickness of PDMS layer. Moreover, Quellmalz *et al* [200] devised a unique transfer and stacking method by application of adhesive bonding with bisbenzocyclobutene (BCB) with the use of a commercial wafer bonding equipment. This enables transfer of CVD grown 2D materials to silicon wafer that is independent of the size and growth substrate. They have also demonstrated the versatility of their protocol by transferring graphene, h-BN and MoS2 and fabricating high performance graphene/h-BN heterostructure FET devices.

5.2.9. Self-powered photodetectors

Self-powered photodetectors essentially allow photodetection without using any external bias. A wide variety of semiconducting nanomaterials such as ZnO, SnO_2, TiO_2, organic and 2D nanomaterials have been proposed for building self-powered photodetectors. Extensive research has been carried out for the design and development of self-powered photodetectors based on different conduction mechanisms such as p-n junction, Schottky junction and photoelectrochemical (PEC)-based photodetectors [201]. Self-powered photodetectors offer several advantages such as suppression of dark current up to ~2 pA due to the absence of an external voltage and rapid optical response owing to fast and efficient e-h pair separation at the p-n junction [202, 203]. Compared to other nanomaterials, 2D materials are best suited for fabricating self-powered photodetectors due to their higher carrier mobility, tunable band gap across the visible to IR range,= and large surface area to capture more light efficiently [204]. There are several excellent reports that have demonstrated 2D material based self-powered photodetectors [205–207], which has also been discussed in section 4.3. There is still tremendous scope in designing more innovative device architectures to enhance the PV effect and improve contact engineering to enable better extraction and separation of charge carriers at the interface.

5.2.10. Other measures for fast photodetection

Development of high-speed photodetectors depends on several factors such as proper band alignment to avoid recombination of photogenerated e-h pairs at the interface, high mobility of the carrier transport layer and efficient contacts. Primarily there are three limiting factors that affect the speed or response time of a photodetector; (a) the diffusion of carriers, (b) transit time in the depletion region, and (c) capacitance of the depletion region. Many effective schemes have been proposed to suppress the recombination at the interface and promote the response speed of 2D material-based photodetectors [208]. Recently, it has been demonstrated that a vdW hetero-diode with a unilateral depletion region configuration and an effective carrier selective contact can greatly reduce the interface trapping effect of the photogenerated carriers and could significantly reduce the

response time [209]. Other critical factors that should be taken into consideration for building fast photodetectors include the selection of correct circuit design and layout to reduce external leakage paths. This could significantly enhance the device performance even at a low input bias and facilitate high-speed optical measurements. For example, a recent work by Thakar *et al* [210] shows how the interface traps and bulk traps in ReS_2 play a different role in the photocurrent generation process, causing a trade-off between responsivity and response time while tuning the gate bias. Two device architectures have been studied; supported ReS_2 and suspended ReS_2. When the supported ReS_2 transistor is in OFF state, the bulk and interface traps are empty. So, upon illumination, these traps play a role in the carrier dynamics, resulting in a slow response speed of 267 s. In the ON state of the phototransistor, the response is lower (4 A W^{-1}) with a response time of milliseconds because of less probability of photogenerated carriers getting trapped in bulk/interface states. In suspended ReS_2 at negative gate bias, there are only bulk trap states that participate in photogating giving rise to a slow response time of 287 s and a low responsivity of 2.2 mA W^{-1}. In ON state of the transistor, the trap states are already occupied, which reduces the responsivity to 1.7 mA W^{-1}. Interestingly, for both device architectures when illumination is turned ON-OFF at a high modulation frequency, response time is in tens of μs, arising from photoconduction effects only. This ensures that it is one of the fastest photodetection devices in the class of individual TMDCs.

6. Conclusion

In summary, photodetection platforms based on Gr and related materials have demonstrated superiority over conventional systems in terms of performance due to their unique properties that govern photophysics. Device architecture and engineering are a crucial aspect for high performance 2D hybrid photodetectors. Challenges remain for commercialization to realize large-scale, high-quality materials and seamless integration with existing photonic and electronic platforms. Indeed, there is substantial potential for vdW heterostructures in the next generation of photodetectors, sensors and in optical communication.

Acknowledgments

The authors acknowledge financial support from U.S. Army International Technology Center Pacific (ITC-PAC) and Ministry of Electronics and Information Technology, Government of India. NC thanks Raman Post-Doc Program, an initiative by Institution of Eminence (IoE) by the Government of India, at Indian Institute of Science, Bangalore. AP thanks Ministry of Human Resource Development, Government of India for the Prime Minister's Research Fellowship.

Data availability statement

All data that support the findings of this study are included within the article (and any supplementary files).

ORCID iDs

Shaili Sett https://orcid.org/0000-0001-6739-8090

References

[1] Zhang K *et al* 2021 Recent progress and challenges based on two-dimensional material photodetectors *Nano Express* **2** 012001
[2] Koppens F H L, Mueller T, Avouris P, Ferrari A C, Vitiello M S and Polini M 2014 Photodetectors based on graphene, other two-dimensional materials and hybrid systems *Nature Nanotechnology* **9** 780–93
[3] Sun Z and Chang H 2014 Graphene and graphene-like two-dimensional materials in photodetection: mechanisms and methodology *ACS Nano* **8** 4133–56
[4] Xia F, Mueller T, Lin Y, Valdes-Garcia A and Avouris P 2009 Ultrafast graphene photodetector *Nature Nanotechnology* **4** 839–43
[5] Yin Z *et al* 2011 Single-layer MoS_2 phototransistors *ACS Nano* **6** 74–80
[6] Huo N, Yang S, Wei Z, Li S-S, Xia J-B and Li J 2014 Photoresponsive and gas sensing field-effect transistors based on multilayer WS_2 nanoflakes *Scientific Reports* **4** 5209
[7] Wei X *et al* 2019 Enhanced photoresponse in $MoTe_2$ photodetectors with asymmetric graphene contacts *Adv. Opt. Mater.* **7** 1900190
[8] Tan Z *et al* 2016 Two-dimensional $(C_4H_9NH_3)_2PbBr_4$ Perovskite crystals for high-performance photodetector *J. Am. Chem. Soc.* **138** 16612–5
[9] Tamalampudi S R *et al* 2014 High performance and bendable few-layered InSe photodetectors with broad spectral response *Nano Lett.* **14** 2800–6
[10] M B, Y N, K S and M A 1991 Photoconduction of black phosphorus in the infrared region. *Japanese Journal of Applied Physics. Part 2. Letters* **30** 1178–81

[11] Ma P et al 2018 Plasmonically enhanced graphene photodetector featuring 100 Gbit/s data reception, high responsivity, and compact size ACS Photonics 6 154–61
[12] Echtermeyer T J et al 2011 Strong plasmonic enhancement of photovoltage in graphene Nature Communications 2 1–5
[13] Lin J, Li H, Zhang H and Chen W 2013 Plasmonic enhancement of photocurrent in MoS_2 field-effect-transistor Appl. Phys. Lett. 102 203109
[14] Ni Z et al 2017 Plasmonic silicon quantum dots enabled high-sensitivity ultrabroadband photodetection of graphene-based hybrid phototransistors ACS Nano 11 9854–62
[15] Konstantatos G et al 2012 Hybrid graphene–quantum dot phototransistors with ultrahigh gain Nature Nanotechnology 7 363–8
[16] Pradhan A et al 2017 Ultra-high sensitivity infra-red detection and temperature effects in a graphene–tellurium nanowire binary hybrid Nanoscale 9 9284–90
[17] Maiti R et al 2020 Strain-engineered high-responsivity $MoTe_2$ photodetector for silicon photonic integrated circuits Nature Photonics 14 578–84
[18] Ma P et al 2018 Fast $MoTe_2$ waveguide photodetector with high sensitivity at telecommunication wavelengths ACS Photonics 5 1846–52
[19] Wang X, Cheng Z, Xu K, Tsang H K and Xu J-B 2013 High-responsivity graphene/silicon-heterostructure waveguide photodetectors Nature Photonics 7 888–91
[20] X D et al 2014 Lateral epitaxial growth of two-dimensional layered semiconductor heterojunctions Nat. Nanotechnol. 9 1024–30
[21] Deng Y et al 2014 Black phosphorus–monolayer MoS_2 van der Waals heterojunction p–n diode ACS Nano 8 8292–9
[22] Flöry N et al 2015 A WSe_2/$MoSe_2$ heterostructure photovoltaic device Appl. Phys. Lett. 107 123106
[23] Amani M et al 2018 Solution-synthesized high-mobility tellurium nanoflakes for short-wave infrared photodetectors ACS Nano 12 7253–63
[24] Xie C and Yan F 2017 Perovskite/Poly(3-hexylthiophene)/graphene multiheterojunction phototransistors with ultrahigh gain in broadband wavelength region ACS Appl. Mater. Interfaces 9 1569–76
[25] Kwak D-H, Lim D-H, Ra H-S, Ramasamy P and Lee J-S 2016 High performance hybrid graphene–$CsPbBr_{3-x}I_x$ perovskite nanocrystal photodetector RSC Adv. 6 65252–6
[26] Castellanos-Gomez A 2015 Black phosphorus: narrow gap, wide applications J. Phys. Chem. Lett. 6 4280–91
[27] Liu E et al 2016 High responsivity phototransistors based on few-layer ReS_2 for weak signal detection Adv. Funct. Mater. 26 1938–44
[28] Nair R R et al 2008 Fine structure constant defines visual transparency of graphene Science 320 1308
[29] Gan X et al 2013 Chip-integrated ultrafast graphene photodetector with high responsivity Nature Photonics 7 883–7
[30] Paria D et al 2015 Ultrahigh field enhancement and photoresponse in atomically separated arrays of plasmonic dimers Adv. Mater. 27 1751–8
[31] Deshpande P, Suri P, Jeong H-H, Fischer P, Ghosh A and Ghosh A 2020 Investigating photoresponsivity of graphene-silver hybrid nanomaterials in the ultraviolet J. Chem. Phys. 152 044709
[32] Britnell L et al 2013 Strong light-matter interactions in heterostructures of atomically thin films Science 340 1311–4
[33] Roy K et al 2013 Graphene-MoS_2 hybrid structures for multifunctional photoresponsive memory devices Nat. Nanotechnol. 8 826–30
[34] Zhang K et al 2016 Interlayer transition and infrared photodetection in atomically thin type-II $MoTe_2$/MoS_2 van der Waals heterostructures ACS Nano 10 3852–8
[35] Flöry N et al 2020 Waveguide-integrated van der Waals heterostructure photodetector at telecom wavelengths with high speed and high responsivity Nature Nanotechnology 15 118–24
[36] Furchi M et al 2012 Microcavity-integrated graphene photodetector Nano Lett. 12 2773–7
[37] Liu Y et al 2011 Plasmon resonance enhanced multicolour photodetection by graphene Nature Communications 2 1–7
[38] Mueller T, Xia F and Avouris P 2010 Graphene photodetectors for high-speed optical communications Nature Photonics 4 297–301
[39] Peng Z, Chen X, Fan Y, Srolovitz D J and Lei D 2020 Strain engineering of 2D semiconductors and graphene: from strain fields to band-structure tuning and photonic applications Light: Science & Applications 9 1–25
[40] Fang H and Hu W 2017 Photogating in low dimensional photodetectors Adv. Sci. 4 1700323
[41] Salehzadeh O, Tran N H, Liu X, Shih I and Mi Z 2014 Exciton kinetics, quantum efficiency, and efficiency droop of monolayer MoS_2 light-emitting devices Nano Lett. 14 4125–30
[42] Dutta R et al 2021 Enhancing carrier diffusion length and quantum efficiency through photoinduced charge transfer in layered graphene-semiconducting quantum dot devices ACS Appl. Mater. Interfaces 13 24295–303
[43] Huang H M, Chang C Y, Hsu Y S, Lu T C, Lan Y P and Lai W C 2012 Enhanced internal quantum efficiency in graphene/InGaN multiple-quantum-well hybrid structures Appl. Phys. Lett. 101 061905
[44] Wang L and Sambur J B 2019 Efficient ultrathin liquid junction photovoltaics based on transition metal dichalcogenides Nano Lett. 19 2960–7
[45] Lu J et al 2020 An asymmetric contact-induced self-powered 2D In2S3 photodetector towards high-sensitivity and fast-response Nanoscale 12 7196–205
[46] Zhou C, Raju S, Li B, Chan M, Chai Y and Yang C Y 2018 Self-driven metal–semiconductor–metal WSe_2 photodetector with asymmetric contact geometries Adv. Funct. Mater. 28 1802954
[47] Li J et al 2016 Tuning the photo-response in monolayer MoS_2 by plasmonic nano-antenna Scientific Reports 6 1–7
[48] Huang L et al 2019 Waveguide-integrated black phosphorus photodetector for mid-infrared applications ACS Nano 13 913–21
[49] Yu W J et al 2013 Highly efficient gate-tunable photocurrent generation in vertical heterostructures of layered materials Nature Nanotechnology 8 952–8
[50] Roy K et al 2018 Number-resolved single-photon detection with ultralow noise van der Waals hybrid Adv. Mater. 30 1704412
[51] Roy K et al 2013 Graphene–MoS_2 hybrid structures for multifunctional photoresponsive memory devices Nature Nanotechnology 8 826–30
[52] Hong X et al 2014 Ultrafast charge transfer in atomically thin MoS_2/WS_2 heterostructures Nature Nanotechnology 9 682–6
[53] Hussain M et al 2021 NIR self-powered photodetection and gate tunable rectification behavior in 2D GeSe/$MoSe_2$ heterojunction diode Scientific Reports 11 1–8
[54] Petritz R L 1956 Theory of photoconductivity in semiconductor films Phys. Rev. 104 1508
[55] Lou Z, Liang Z and Shen G 2016 Photodetectors based on two dimensional materials* J. Semiconduct. 37 091001
[56] Qiu Q and Huang Z 2021 Photodetectors of 2D materials from ultraviolet to terahertz waves Adv. Mater. 33 2008126
[57] Richards P L 1998 Bolometers for infrared and millimeter waves J. Appl. Phys. 76 1
[58] Wang L et al 2018 2D photovoltaic devices: progress and prospects Small Methods 2 1700294
[59] Rose Albert 1963 Concepts in Photoconductivity and Allied problems (Interscience Publishers)

[60] Buscema M *et al* 2015 Photocurrent generation with two-dimensional van der Waals semiconductors *Chem. Soc. Rev.* **44** 3691–718
[61] Thylén L and Wosinski L 2014 Integrated photonics in the 21st century *Photonics Research* **2** 75–81
[62] Furchi M M, Polyushkin D K, Pospischil A and Mueller T 2014 Mechanisms of photoconductivity in atomically thin MoS_2 *Nano Lett.* **14** 6165–70
[63] Pradhan N R *et al* 2015 High photoresponsivity and short photoresponse times in few-layered WSe_2 transistors *ACS Appl. Mater. Interfaces* **7** 12080–8
[64] Pradhan N R *et al* 2015 Hall and field-effect mobilities in few layered p-WSe_2 field-effect transistors *Scientific Reports* **5** 1–8
[65] Suess R J *et al* 2016 Mid-infrared time-resolved photoconduction in black phosphorus *2D Mater.* **3** 041006
[66] Liu F *et al* 2016 Highly sensitive detection of polarized light using anisotropic 2D ReS_2 *Adv. Funct. Mater.* **26** 1169–77
[67] Baugher B W H, Churchill H O H, Yang Y and Jarillo-Herrero P 2014 Optoelectronic devices based on electrically tunable p–n diodes in a monolayer dichalcogenide *Nature Nanotechnology* **9** 262–7
[68] Gabor N M *et al* 2011 Hot carrier-assisted intrinsic photoresponse in graphene *Science* **334** 648–52
[69] Yan J *et al* 2012 Dual-gated bilayer graphene hot-electron bolometer *Nat. Nanotechnol.* **7** 472–8
[70] Yuan S *et al* 2020 Room temperature graphene mid-infrared bolometer with a broad operational wavelength range *ACS Photonics* **7** 1206–15
[71] Memaran S *et al* 2015 Pronounced photovoltaic response from multilayered transition-metal dichalcogenides PN-junctions *Nano Lett.* **15** 7532–8
[72] Wang Z *et al* 2016 Electrostatically tunable lateral $MoTe_2$ p–n junction for use in high-performance optoelectronics *Nanoscale* **8** 13245–50
[73] Buscema M, Groenendijk D J, Blanter S I, Steele G A, van der Zant H S J and Castellanos-Gomez A 2014 Fast and broadband photoresponse of few-layer black phosphorus field-effect transistors *Nano Lett.* **14** 3347–52
[74] Liu Y, Cai Y, Zhang G, Zhang Y-W and Ang K-W 2017 Al-doped black phosphorus p–n homojunction diode for high performance photovoltaic *Adv. Funct. Mater.* **27** 1604638
[75] Yu X, Zhang S, Zeng H and Wang Q J 2016 Lateral black phosphorene P–N junctions formed via chemical doping for high performance near-infrared photodetector *Nano Energy* **25** 34–41
[76] MY L *et al* 2015 NANOELECTRONICS. Epitaxial growth of a monolayer WSe_2-MoS_2 lateral p-n junction with an atomically sharp interface *Science (New York, N.Y.)* **349** 524–8
[77] Lee J Y, Shin J-H, Lee G-H and Lee C-H 2016 Two-dimensional semiconductor optoelectronics based on van der Waals heterostructures *Nanomaterials* **6** 193
[78] Cheng R *et al* 2014 Electroluminescence and photocurrent generation from atomically sharp WSe_2/MoS_2 heterojunction p–n diodes *Nano Lett.* **14** 5590–7
[79] Lee H S, Ahn J, Shim W, Im S and Hwang D K 2018 2D WSe_2/MoS_2 van der Waals heterojunction photodiode for visible-near infrared broadband detection *Appl. Phys. Lett.* **113** 163102
[80] Li X *et al* 2016 Two-dimensional GaSe/$MoSe_2$ misfit bilayer heterojunctions by van der Waals epitaxy *Sci. Adv.* **2**
[81] Choudhary N *et al* 2016 Centimeter scale patterned growth of vertically stacked few layer only 2D MoS_2/WS_2 van der Waals heterostructure *Scientific Reports* **6** 1–7
[82] Liu H *et al* 2019 Self-powered broad-band photodetectors based on vertically stacked WSe_2/Bi_2Te_3 p-n heterojunctions *ACS Nano* **13** 13573–80
[83] Wadhwa R, Agrawal A V, Kushavah D, Mushtaq A, Pal S K and Kumar M 2021 Investigation of charge transport and band alignment of MoS_2-ReS_2 heterointerface for high performance and self-driven broadband photodetection *Appl. Surf. Sci.* **569** 150949
[84] Ahn J *et al* 2021 2D $MoTe_2/ReS_2$ van der Waals heterostructure for high-performance and linear polarization-sensitive photodetector *ACS Photonics* **8** 2650–8
[85] Long M *et al* 2016 Broadband photovoltaic detectors based on an atomically thin heterostructure *Nano Lett.* **16** 2254–9
[86] Wang Q, Zhou C and Chai Y 2020 Breaking symmetry in device design for self-driven 2D material based photodetectors *Nanoscale* **12** pp 8109–18 Royal Society of Chemistry
[87] Huang H *et al* 2016 Highly sensitive visible to infrared $MoTe_2$ photodetectors enhanced by the photogating effect *Nanotechnology* **27** 445201
[88] Gao S *et al* 2021 Graphene/MoS_2/graphene vertical heterostructure-based broadband photodetector with high performance *Adv. Mater. Interfaces* **8** 2001730
[89] Liu B *et al* 2019 High performance photodetector based on graphene/MoS2/graphene lateral heterostrurcture with Schottky junctions *J. Alloys Compd.* **779** 140–6
[90] Gao W *et al* 2021 2D WS_2 based asymmetric schottky photodetector with high performance *Adv. Electron. Mater.* **7** 2000964
[91] Ning J *et al* 2020 Self-driven photodetector based on a GaSe/$MoSe_2$ selenide van der Waals heterojunction with the hybrid contact *Appl. Phys. Lett.* **117** 163104
[92] Hussain M *et al* 2020 Asymmetric electrode incorporated 2D GeSe for self-biased and efficient photodetection *Scientific Reports* **10** 1–8
[93] Freitag M, Low T, Xia F and Avouris P 2012 Photoconductivity of biased graphene *Nature Photonics* **7** 53–9
[94] Kruse P W 2009 *Uncooled Thermal Imaging Arrays, Systems, and Applications* (SPIE Press)
[95] Efetov D K *et al* 2018 Fast thermal relaxation in cavity-coupled graphene bolometers with a Johnson noise read-out *Nature Nanotechnology* **13** 797–801
[96] Groenendijk D J *et al* 2014 Photovoltaic and photothermoelectric effect in a double-gated WSe_2 device *Nano Lett.* **14** 5846–52
[97] Wang Q *et al* 2019 Anomalous photothermoelectric transport due to anisotropic energy dispersion in WTe_2 *Nano Lett.* **19** 2647–52
[98] Zhang Y *et al* 2015 Photothermoelectric and photovoltaic effects both present in MoS_2 *Scientific Reports* **5** 1–7
[99] Schuler S *et al* 2016 Controlled generation of a p–n junction in a waveguide integrated graphene photodetector *Nano Lett.* **16** 7107–12
[100] Soci† C *et al* 2007 ZnO nanowire UV photodetectors with high internal gain *Nano Lett.* **7** 1003–9
[101] Sett S, Ghatak A, Sharma D, Kumar G V P and Raychaudhuri A K 2018 Broad band single germanium nanowire photodetectors with surface oxide-controlled high optical gain *J. Phys. Chem.* C **122** 8564–72
[102] Zhang W, Huang J-K, Chen C-H, Chang Y-H, Cheng Y-J and Li L-J 2013 High-gain phototransistors based on a CVD MoS_2 monolayer *Adv. Mater.* **25** 3456–61
[103] Island J O, Blanter S I, Buscema M, van der Zant H S J and Castellanos-Gomez A 2015 Gate controlled photocurrent generation mechanisms in high-gain In_2Se_3 phototransistors *Nano Lett.* **15** 7853–8
[104] Guo Q *et al* 2016 Black phosphorus mid-infrared photodetectors with high gain *Nano Lett.* **16** 4648–55
[105] Ahmed T, Roy K, Kakkar S, Pradhan A and Ghosh A 2020 Interplay of charge transfer and disorder in optoelectronic response in Graphene/hBN/MoS_2 van der Waals heterostructures *2D Mater.* **7** 025043

[106] Liu C H, Chang Y C, Norris T B and Zhong Z 2014 Graphene photodetectors with ultra-broadband and high responsivity at room temperature *Nat. Nanotechnol.* **9** 273–8
[107] Qiao H *et al* 2015 Broadband photodetectors based on graphene-Bi_2Te_3 heterostructure *ACS Nano* **9** 1886–94
[108] Roy K, Padmanabhan M, Goswami S, Sai T P, Kaushal S and Ghosh A 2013 Optically active heterostructures of graphene and ultrathin MoS_2 *Solid State Commun.* **175–176** 35–42
[109] Liu B *et al* 2019 High responsivity and near-infrared photodetector based on graphene/$MoSe_2$ heterostructure *Chinese Optics Letters* **17** 020002
[110] Zhang W *et al* 2015 Ultrahigh-gain photodetectors based on atomically thin graphene-MoS_2 heterostructures *Sci. Rep.* **4** 1–8
[111] Mitra S, Kakkar S, Ahmed T and Ghosh A 2020 Graphene- WS_2 van der Waals hybrid heterostructure for photodetector and memory device applications *Phys. Rev. Appl.* **14** 064029
[112] Kashid R *et al* 2020 Observation of inter-layer charge transmission resonance at optically excited graphene–TMDC interfaces *APL Mater.* **8** 091114
[113] Zhao Y *et al* 2021 Graphene/SnS_2 van der Waals photodetector with high photoresponsivity and high photodetectivity for broadband 365–2240 nm detection *ACS Appl. Mater. Interfaces* **13** 47198–207
[114] Kasani S, Curtin K and Wu N 2019 A review of 2D and 3D plasmonic nanostructure array patterns: fabrication, light management and sensing applications *Nanophotonics* **8** 2065–89
[115] Fang Z, Liu Z, Wang Y, Ajayan P M, Nordlander P and Halas N J 2012 Graphene-antenna sandwich photodetector *Nano Lett.* **12** 3808–13
[116] Miao J *et al* 2015 Surface plasmon-enhanced photodetection in few layer MoS_2 phototransistors with Au nanostructure arrays *Small* **11** 2392–8
[117] Ren H, Chen J-D, Li Y-Q and Tang J-X 2021 Recent progress in organic photodetectors and their applications *Adv. Sci.* **8** 2002418
[118] Zhao Z, Xu C, Niu L, Zhang X and Zhang F 2020 Recent progress on broadband organic photodetectors and their applications *Laser Photonics Rev.* **14** 2000262
[119] Li H *et al* 2020 Recent progress and strategies in photodetectors based on 2D inorganic/organic heterostructures *2D Mater.* **8** 012001
[120] Liu X *et al* 2016 Epitaxial ultrathin organic crystals on graphene for high-efficiency phototransistors *Adv. Mater.* **28** 5200–5
[121] Han J *et al* 2018 Graphene/organic semiconductor heterojunction phototransistors with broadband and bi-directional photoresponse *Adv. Mater.* **30** 1804020
[122] Kang D H *et al* 2016 An ultrahigh-performance photodetector based on a Perovskite–transition-metal-dichalcogenide hybrid structure *Adv. Mater.* **28** 7799–806
[123] Cai B, Zhao Y, Zhang Z and Ouyang G 2021 Interfacial charge transfer and photovoltaic properties in C60/MoS_2 0D–2D van der Waals heterostructures *Physica Status Solidi (RRL)—Rapid Research Letters* **15** 2100311
[124] Wang X *et al* 2019 Multimechanism synergistic photodetectors with ultrabroad spectrum response from 375 nm to 10 μm *Adv. Sci.* **6** 1901050
[125] Homan S B, Sangwan V K, Balla I, Bergeron H, Weiss E A and Hersam M C 2017 Ultrafast exciton dissociation and long-lived charge separation in a photovoltaic pentacene-MoS_2 van der Waals heterojunction *Nano Lett.* **17** 164–9
[126] Shiue R-J *et al* 2015 High-responsivity graphene–boron nitride photodetector and autocorrelator in a silicon photonic integrated circuit *Nano Lett.* **15** 7288–93
[127] Guo J *et al* 2020 High-performance silicon-graphene hybrid plasmonic waveguide photodetectors beyond 1.55 μm *Light: Science & Applications* **9** 1–11
[128] Marconi S *et al* 2021 Photo thermal effect graphene detector featuring 105 Gbit s−1 NRZ and 120 Gbit s−1 PAM4 direct detection *Nature Communications* **12** 1–10
[129] Youngblood N, Chen C, Koester S J and Li M 2015 Waveguide-integrated black phosphorus photodetector with high responsivity and low dark current *Nature Photonics* **9** 247–52
[130] Geim A K and Grigorieva I. v. 2013 Van der Waals heterostructures *Nature* **499** 419–25
[131] di Bartolomeo A 2020 Emerging 2D materials and their Van Der Waals heterostructures *Nanomaterials* **10** 579
[132] Lu X, Sun L, Jiang P and Bao X 2019 Progress of photodetectors based on the photothermoelectric effect *Adv. Mater.* **31** 1902044
[133] Cai X *et al* 2014 Sensitive room-temperature terahertz detection via the photothermoelectric effect in graphene *Nat. Nanotechnol.* **9** 814–9
[134] Cai X *et al* 2015 Plasmon-enhanced Terahertz photodetection in graphene *Nano Lett.* **15** 4295–302
[135] Jung M, Rickhaus P, Zihlmann S, Makk P and Schönenberger C 2016 Microwave photodetection in an ultraclean suspended bilayer graphene p-n junction *Nano Lett.* **16** 6988–93
[136] Lee G H *et al* 2020 Graphene-based Josephson junction microwave bolometer *Nature* **586** 42–6
[137] Haller R *et al* Phase-dependent microwave response of a graphene Josephson junction,' Aug. 2021, [Online]. Available: http://arxiv.org/abs/2108.00989
[138] Kokkoniemi R *et al* 2020 Bolometer operating at the threshold for circuit quantum electrodynamics *Nature* **586** 47–51
[139] Kang D H *et al* 2016 An ultrahigh-performance photodetector based on a Perovskite–transition-metal-dichalcogenide hybrid structure *Adv. Mater.* **28** 7799–806
[140] Wen W, Zhang W, Wang X, Feng Q, Liu Z and Yu T 2021 Ultrasensitive photodetectors promoted by interfacial charge transfer from layered Perovskites to chemical vapor deposition-grown MoS_2 *Small* **17** 2102461
[141] Yang Z *et al* 2017 Wafer-scale synthesis of high-quality semiconducting two-dimensional layered InSe with broadband photoresponse *ACS Nano* **11** 4225–36
[142] Feng W *et al* 2015 Ultrahigh photo-responsivity and detectivity in multilayer InSe nanosheets phototransistors with broadband response *J. Mater. Chem.* C **3** 7022–8
[143] Sharma A, Bhattacharyya B, Srivastava A K, Senguttuvan T D and Husale S 2016 High performance broadband photodetector using fabricated nanowires of bismuth selenide *Scientific Reports* **6** 1–8
[144] Konstantatos G 2018 Current status and technological prospect of photodetectors based on two-dimensional materials *Nature Communications* **9** 1–3
[145] Deng B *et al* 2020 Strong mid-infrared photoresponse in small-twist-angle bilayer graphene *Nature Photonics* **14** 549–53
[146] Jin C *et al* 2019 Observation of moiré excitons in WSe_2/WS_2 heterostructure superlattices *Nature* **567** 76–80
[147] Tran K *et al* 2019 Evidence for moiré excitons in van der Waals heterostructures *Nature* **567** 71–5
[148] Yu H, bin Liu G, Tang J, Xu X and Yao W 2017 Moiré excitons: from programmable quantum emitter arrays to spin-orbit–coupled artificial lattices *Sci. Adv.* **3** e1701696
[149] Baek H *et al* 2020 Highly energy-tunable quantum light from moiré-trapped excitons *Sci. Adv.* **6** 8526–37

[150] Sefidmooye Azar N et al 2021 Long-wave infrared photodetectors based on 2D platinum diselenide atop optical cavity substrates ACS Nano 15 6573–81
[151] You C et al 2021 Design and performance study of hybrid graphene/HgCdTe mid-infrared photodetector IEEE Sens. J. 21 1–1
[152] Li F et al 2020 HgCdTe mid-Infrared photo response enhanced by monolithically integrated meta-lenses Scientific Reports 10 1–10
[153] Hu W et al 2019 Germanium/perovskite heterostructure for high-performance and broadband photodetector from visible to infrared telecommunication band Light: Science & Applications 8 1–10
[154] Zhou Y, Tan H, Sheng Y, Fan Y, Xu W and Warner J H 2018 Utilizing interlayer excitons in bilayer WS_2 for increased photovoltaic response in ultrathin graphene vertical cross-bar photodetecting tunneling transistors ACS Nano 12 4669–77
[155] Jiang Z et al 2021 Ultraflexible integrated organic electronics for ultrasensitive photodetection Adv. Mater. Technol. 6 e1701696
[156] Kozawa D et al 2016 Evidence for fast interlayer energy transfer in $MoSe_2/WS_2$ heterostructures Nano Lett. 16 4087–93
[157] Froehlicher G, Lorchat E and Berciaud S 2018 Charge versus energy transfer in atomically thin graphene-transition metal dichalcogenide van der Waals heterostructures Phys. Rev. X 8 011007
[158] Xu Z, Liu Z, Zhang D, Zhong Z and Norris T B 2021 Ultrafast dynamics of charge transfer in CVD grown MoS_2–graphene heterostructure Appl. Phys. Lett. 119 093102
[159] Lim D U, Jo S B and Cho J H 2021 Cold-trap-mediated broad dynamic photodetection in graphene–organic hybrid photonic barristors J. Am. Chem. Soc. 143 879–90
[160] Cai Z, Cao M, Jin Z, Yi K, Chen X and Wei D 2018 Large photoelectric-gating effect of two-dimensional van-der-Waals organic/tungsten diselenide heterointerface npj 2D Materials and Applications 2 1–7
[161] Liu J, Liang Q, Zhao R, Lei S and Hu W 2020 Application of organic–graphene hybrids in high performance photodetectors Mater. Chem. Front. 4 354–68
[162] Fang Y, Armin A, Meredith P and Huang J 2018 Accurate characterization of next-generation thin-film photodetectors Nature Photonics 13 1–4
[163] Ghosh A, Kar S, Bid A and Raychaudhuri A K 2021 A set-up for measurement of low frequency conductance fluctuation (noise) using digital signal processing techniques (https://arxiv.org/abs/cond-mat/0402130v1)
[164] Karnatak P, Sai T P, Goswami S, Ghatak S, Kaushal S and Ghosh A 2016 Current crowding mediated large contact noise in graphene field-effect transistors Nature Communications 7 1–8
[165] Kakkar S, Karnatak P, Aamir M A, Watanabe K, Taniguchi T and Ghosh A 2020 Optimal architecture for ultralow noise graphene transistors at room temperature Nanoscale 12 17762–8
[166] Ouyang T, Wang X, Liu S, Chen H and Deng S 2021 A complete two-dimensional avalanche photodiode based on $MoTe_2-WS_2-MoTe_2$ heterojunctions with ultralow dark current Frontiers in Materials 8 303
[167] Wang H et al 2020 Extremely low dark current MoS_2 photodetector via 2D halide perovskite as the electron reservoir Adv. Opt. Mater. 8 1901402
[168] Pak Y et al 2020 Dark-current reduction accompanied photocurrent enhancement in p-type MnO quantum-dot decorated n-type 2D-MoS_2-based photodetector Appl. Phys. Lett. 116 112102
[169] Long M, Wang P, Fang H and Hu W 2019 Progress, challenges, and opportunities for 2D material based photodetectors Adv. Funct. Mater. 29 1803807
[170] Guo Q et al 2018 Efficient electrical detection of mid-infrared graphene plasmons at room temperature Nature Materials 17 986–92
[171] Yuan S et al 2018 Air-stable room-temperature mid-infrared photodetectors based on hBN/black arsenic phosphorus/hBN heterostructures Nano Lett. 18 3172–9
[172] Deckoff-Jones S, Wang Y, Lin H, Wu W and Hu J 2019 'Tellurene: a multifunctional material for midinfrared optoelectronics ACS Photonics 6 1632–8
[173] Bullock J, Amani M, Cho J et al 2018 Polarization-resolved black phosphorus/molybdenum disulfide mid-wave infrared photodiodes with high detectivity at room temperature Nature Photon 12 601–7
[174] Miao J and Wang C 2021 Avalanche photodetectors based on two-dimensional layered materials Nano Res. 14 pp 1878–88 Tsinghua University
[175] Wang H et al 2021 Emerging single-photon detectors based on low-dimensional materials Small 1 2103963 New York Wiley
[176] Lei S et al 2015 An atomically layered InSe avalanche photodetector Nano Lett. 15 3048–55
[177] Jia J, Jeon J, Park J-H, Lee B H, Hwang E and Lee S 2019 Black phosphorus: avalanche carrier multiplication in multilayer black phosphorus and avalanche photodetector (small 38/2019) Small 15 1970203
[178] Gao A et al 2019 Observation of ballistic avalanche phenomena in nanoscale vertical InSe/BP heterostructures Nat. Nanotechnol. 14 217–22
[179] Seo J et al 2021 Ultrasensitive photodetection in MoS_2 avalanche phototransistors Adv. Sci. 2102437
[180] Sangwan V K et al 2020 Intrinsic carrier multiplication in layered Bi_2O_2Se avalanche photodiodes with gain bandwidth product exceeding 1 GHz Nano Research 14 1961–6
[181] Liu L et al 2014 Heteroepitaxial growth of two-dimensional hexagonal boron nitride templated by graphene edges Science (New York, N.Y.) 343 163–7
[182] Kim S M et al 2013 Synthesis of patched or stacked graphene and hBN flakes: a route to hybrid structure discovery Nano Lett. 13 933–41
[183] Zhang Y et al 2015 All chemical vapor deposition synthesis and intrinsic bandgap observation of MoS_2/graphene heterostructures Adv. Mater. 27 7086–92
[184] Zhang Z, Chen P, Duan X, Zang K, Luo J and Duan X 2017 Robust epitaxial growth of two-dimensional heterostructures, multiheterostructures, and superlattices Science 357 788–92
[185] Zhang T and Fu L 2018 Controllable chemical vapor deposition growth of two-dimensional heterostructures Chem 4 671–89
[186] Jin G et al 2021 Heteroepitaxial van der Waals semiconductor superlattices Nature Nanotechnology 16 1092–8
[187] Gong Y et al 2014 Vertical and in-plane heterostructures from WS_2/MoS_2 monolayers Nat. Mater. 13 1135–42
[188] Yang L, Chen W, Yu Q and Liu B 2020 Mass production of two-dimensional materials beyond graphene and their applications Nano Research 14 1583–97
[189] Zhang C et al 2020 Mass production of 2D materials by intermediate-assisted grinding exfoliation Natl Sci. Rev. 7 324–32
[190] Indra Alzakia F, Jonhson W, Ding J and Ching Tan S 2020 Ultrafast exfoliation of 2D materials by solvent activation and one-step fabrication of all-2D-material photodetectors by electrohydrodynamic printing Cite This: ACS Appl. Mater. Interfaces 12 28840–51
[191] Sebastian A, Pendurthi R, Choudhury T H, Redwing J M and Das S 2021 Benchmarking monolayer MoS_2 and WS_2 field-effect transistors Nat. Commun. 12 1–12
[192] Akinwande D et al 2019 Graphene and two-dimensional materials for silicon technology Nature 573 507–18

[193] Kong X et al 2019 Graphene/Si Schottky solar cells: a review of recent advances and prospects RSC Adv. 9 863–77
[194] Chen X et al 2020 Graphene hybrid structures for integrated and flexible optoelectronics Adv. Mater. 32 1902039
[195] Wirth-Lima A J, Alves-Sousa P P and Bezerra-Fraga W 2019 Graphene/silicon and 2D-MoS_2/silicon solar cells: a review Applied Physics A: Materials Science and Processing 125 1–21
[196] Kim C, Yoon M-A, Jang B, Kim J-H and Kim K-S 2020 A review on transfer process of two-dimensional materials Tribology and Lubricants 36 1–10
[197] Shen P C et al 2018 CVD technology for 2D materials IEEE Trans. Electron Devices 65 4040–52
[198] Watson A J, Lu W, Guimaraes M H D and Stöhr M 2021 Transfer of large-scale two-dimensional semiconductors: challenges and developments 2D Mater. 8 032001
[199] Kim C et al 2021 Damage-free transfer mechanics of 2-dimensional materials: competition between adhesion instability and tensile strain NPG Asia Materials 13 1–11
[200] Quellmalz A et al 2021 Large-area integration of two-dimensional materials and their heterostructures by wafer bonding Nature Communications 12 1–11
[201] Qiao H et al 2020 Self-powered photodetectors based on 2D materials Adv. Opt. Mater. 8 1900765
[202] Mao Y et al 2021 Self-powered high-detectivity lateral MoS_2 Schottky photodetectors for near-infrared operation Adv. Electron. Mater. 7 2001138
[203] Gui P et al 2020 Self-driven all-inorganic perovskite microplatelet vertical Schottky junction photodetectors with a tunable spectral response J. Mater. Chem. C 8 6804–12
[204] Jiang J et al 2021 Recent advances in 2D materials for photodetectors Adv. Electron. Mater. 7 2001125
[205] Periyanagounder D, Gnanasekar P, Varadhan P, He J-H and Kulandaivel J 2018 High performance, self-powered photodetectors based on a graphene/silicon Schottky junction diode J. Mater. Chem. C 6 9545–51
[206] Ahn J et al 2020 Self-powered visible–invisible multiband detection and imaging achieved using high-performance 2D $MoTe_2/MoS_2$ semivertical heterojunction photodiodes ACS Appl. Mater. Interfaces 12 10858–66
[207] Zou Z et al 2021 Liquid-metal-assisted growth of vertical GaSe/MoS_2 p–n heterojunctions for sensitive self-driven photodetectors ACS Nano 15 10039–47
[208] Mehew J D et al 2017 Fast and highly sensitive ionic-polymer-gated WS_2–graphene photodetectors Adv. Mater. 29 1700222
[209] Wu F et al 2019 High efficiency and fast van der Waals hetero-photodiodes with a unilateral depletion region Nat. Commun. 10 1–8
[210] Thakar K, Mukherjee B, Grover S, Kaushik N, Deshmukh M and Lodha S 2018 Multilayer ReS_2 photodetectors with gate tunability for high responsivity and high-speed applications ACS Appl. Mater. Interfaces 10 36512–22
[211] Liu Y, Shivananju B N, Wang Y, Zhang Y, Yu W, Xiao S and Bao Q 2017 Highly efficient and air-stable infrared photodetector based on 2D layered graphene–black phosphorus heterostructure ACS Appl. Mater. Interfaces 9 36137–45
[212] Fu L, Wang F, Wu B, Wu N, Huang W, Wang H and Liu Y 2017 Van der Waals epitaxial growth of atomic layered HfS2 crystals for ultrasensitive near-infrared phototransistors Adv. Mater. 29 1700439
[213] Zhu X, Shi L, Schmidt M S, Boisen A, Hansen O, Zi J and Mortensen N A 2013 Enhanced light–matter interactions in graphene-covered gold nanovoid arrays Nano Lett. 13 4690–6
[214] Zhang Y, You Q, Huang W, Hu L, Ju J, Ge Y and Zhang H 2020 Few-layer hexagonal bismuth telluride (Bi_2Te_3) nanoplates with high-performance UV-Vis photodetection Nanoscale Advances 2 1333–9
[215] Liu F, Chow W L, He X, Hu P, Zheng S, Wang X, Zhou J, Fu Q, Fu W, Yu P, Zeng Q, Fan H J, Tay B K, Kloc C and Liu Z 2015 Van der Waals p-n Junction Based on an Organic-Inorganic Heterostructure Advanced Functional Materials 25 5865–71
[216] Islam S, Mishra J K, Kumar A, Chatterjee D, Ravishankar N and Ghosh A 2019 Ultra-sensitive graphene–bismuth telluride nano-wire hybrids for infrared detection Nanoscale 11 1579–86